 doi:10.20944/preprints202009.0366.v1

Three-dimensional modeling and fluid flow simulation for the quantitative description of permeability anisotropy in tidal flat carbonate

Hassan A. Eltom Nabil A. Saraih, Oliver G. Esteva, Lundi Kusuma, Saleh Ahmed, and Mohamed A. Yassin

Geosciences Department, College of Petroleum Engineering & Geosciences, King Fahd University of Petroleum & Minerals, Building 76, Dhahran, 31261, KSA

**Corresponding author email address: hassan.eltom@kfupm.edu.sa*

Abstract

Three-dimensional (3D) facies and petrophysical models were generated from previously published data of carbonate strata in the Dam Formation (eastern Saudi Arabia) to quantitatively investigate, describe, understand, model, and predict the permeability anisotropy of tidal flat carbonate within a sequence stratigraphic framework. The resulting 3D models were used to conduct fluid flow simulations to demonstrate how permeability anisotropy influences the production of hydrocarbons and ultimately affects decisions concerning future drilling in the exploration and development of carbonate reservoirs that have tidal flat strata. The constructed 3D facies model consists of four lithofacies associations, two of which were grain-dominated associations and two of which were mud-dominated associations. These lithofacies associations varied spatially in four reservoir zones (zones 1 to 4), which represent two fourth-order sequences in the uppermost part of the Dam Formation. Zones 1 and 3 consist of transgressive parasequences, and zones 2 and 4 consist of the regressive parasequences of these sequences. The 3D porosity and permeability models have a coherent match with the distribution of the lithofacies and the stratigraphic framework of the Dam Formation. The results suggested that the permeability anisotropy in zones 1 and 3 is controlled by the occurrence of the grain-dominated lithofacies

 doi:10.20944/preprints202009.0366.v1

associated with tidal flat channels. This lithofacies association overlies the sequence boundaries of sequences 1 and 3, forms reservoir bodies with relatively high permeability values, and is elongated perpendicular to the shoreline of the depositional environments. In contrast, permeability anisotropy in zones 2 and 4 is thought to be controlled by the occurrence of the grain-dominated lithofacies associated with the oolitic shoal. This lithofacies association overlies the maximum flooding surface of sequences 2 and 4, forms reservoir bodies with relatively high permeability values, and is elongated parallel to the shoreline of the depositional environments. Fluid flow simulation results suggested that the trend in hydrocarbon production from the constructed 3D models depends on permeability anisotropy in each reservoir zone. Thus, recognizing trends in permeability anisotropy, which might be predicted using sequences stratigraphy, could help to identify potential areas for future drilling.

Keywords

outcrop reservoir analog; tidal flat; reservoir performance; future drilling, reservoir quality prediction

1. Introduction

Anisotropy of properties in porous media is defined as the variation in those properties based on direction (Pickup et al., 1995). Thus, such properties depend on the location and orientation in a porous medium (Zhang et al., 2008; Branets et al., 2009). Isotropy, the opposite term, implies that the physical properties of the porous medium are not directionally dependent (Zhang et al., 2008; Branets et al., 2009). The permeability (the ease with which a fluid flows through rocks) of the sedimentary strata usually is considered to be an anisotropic physical property because of the considerable vertical and horizontal variation in its values (Branets et al., 2009). Recognizing and

 doi:10.20944/preprints202009.0366.v1

analyzing the controls on permeability anisotropy is very important to optimize the fluid flow performance in hydrocarbon reservoirs and water aquifers and to locate sides for the storage of carbon dioxide.

In tidal flat carbonate, permeability anisotropy results from the interfingering of the heterogeneous facies mosaic (Shinn et al., 1969; Grover and Read, 1978; Shinn, 1983; Pratt and JAMES, 1986; Read et al., 1986; Rankey, 2002; Rankey and Morgan, 2002). Therefore, distinguishing the spatial and temporal patterns of sedimentary strata in the rock record provides insights into the controls on the permeability anisotropy in subsurface reservoirs (Meyer et al., 1996; Amour et al., 2011; Purkis and Vlaswinkel, 2012; Eltom et al., 2013; Stanley et al., 2014; Rankey et al., 2018). Previous works in modern tidal flat environments and in their equivalent strata in the rock record have recognized various geological parameters that can be used to develop predictive facies models that facilitate the understanding of permeability anisotropy in these environments (Verwer et al., 2009; Palermo et al., 2010; Amour et al., 2011; Petrovic et al., 2018). Most of the previous works were centered on qualitative descriptions, such as the sedimentological, stratigraphic, and diagenetic characteristics, but the quantitative descriptions have been given less attention.

In this context, the objective of this study is to investigate illustrative outcrops of tidal flat carbonate (Dam Formation) in the Lidam area of eastern Saudi Arabia to enhance the quantitative descriptions and to understand the controls on permeability anisotropy in carbonate reservoirs of tidal flat settings. Through generating 3D facies and petrophysical models and running fluid flow simulations on these models, this effort recognized trends in the spatial variability of sedimentary strata, permeability and porosity, and hydrocarbon production within sequence stratigraphic framework. Therefore, the results provide perceptions that facilitate the understanding of the

Preprints (www.preprints.org) | NOT PEER-REVIEWED | Posted: 16 September 2020 doi:10.20944/preprints202009.0366.v1

controls on permeability anisotropy that influence fluid flow behaviors in subsurface reservoirs with tidal flat carbonate.

2. Study area and geological background

The Early Miocene (Burdigalian) Dam Formation cropped out in the Al-Lidam area (26° 21′ 42″ N, 49° 27′ 42″ E) approximately 80 km west of Dammam in the Eastern Province of Saudi Arabia (Fig. 1). The formation was described first by Steineke and Koch (1935) as strata that consist of carbonate rocks, and, based on its lithological characteristics, fossil contents, and stratigraphic pattern, these strata were interpreted to have been deposited in tidal flat settings (Powers et al., 1966; Iriem, 1987; Alkhaldi, 2009; Ali, 2015; Bashri et al., 2017; Abdelkarim et al., 2019). The strata of the Dam Formation are exposed in the study area as a series of connected and disconnected escarpments with a general trend in the NNW-SSE directions (Fig. 1C). Stratigraphically, the Dam Formation (which is ~100 m thick) overlies the Hofuf Formation and is overlain by the Hadruk Formation (Fig. 1B) (Powers et al., 1966; Weijermars, 1999). In the study area, only the uppermost part of the Dam Formation is exposed (Fig. 1C, Powers et al., 1966; Iriem, 1987). Recent studies (Alkhaldi, 2009; Ali, 2015) have divided the exposed strata of the Dam Formation in the Al-Lidam area into several high-frequency sequences. (See section 3 for more details).

3. Data

3.1. Location

The input data for the geostatistical models in this study came from previous works (Alkhaldi, 2009; Ali, 2015; Bashri et al., 2017; Abdelkarim et al., 2019). These works investigated 26

Preprints (www.preprints.org) | NOT PEER-REVIEWED | Posted: 16 September 2020 doi:10.20944/preprints202009.0366.v1

outcrops in the study area (Fig. 1C), and 14 outcrops were selected to be measured in detail. These 14 outcrops represent two transects (Fig. 1C).

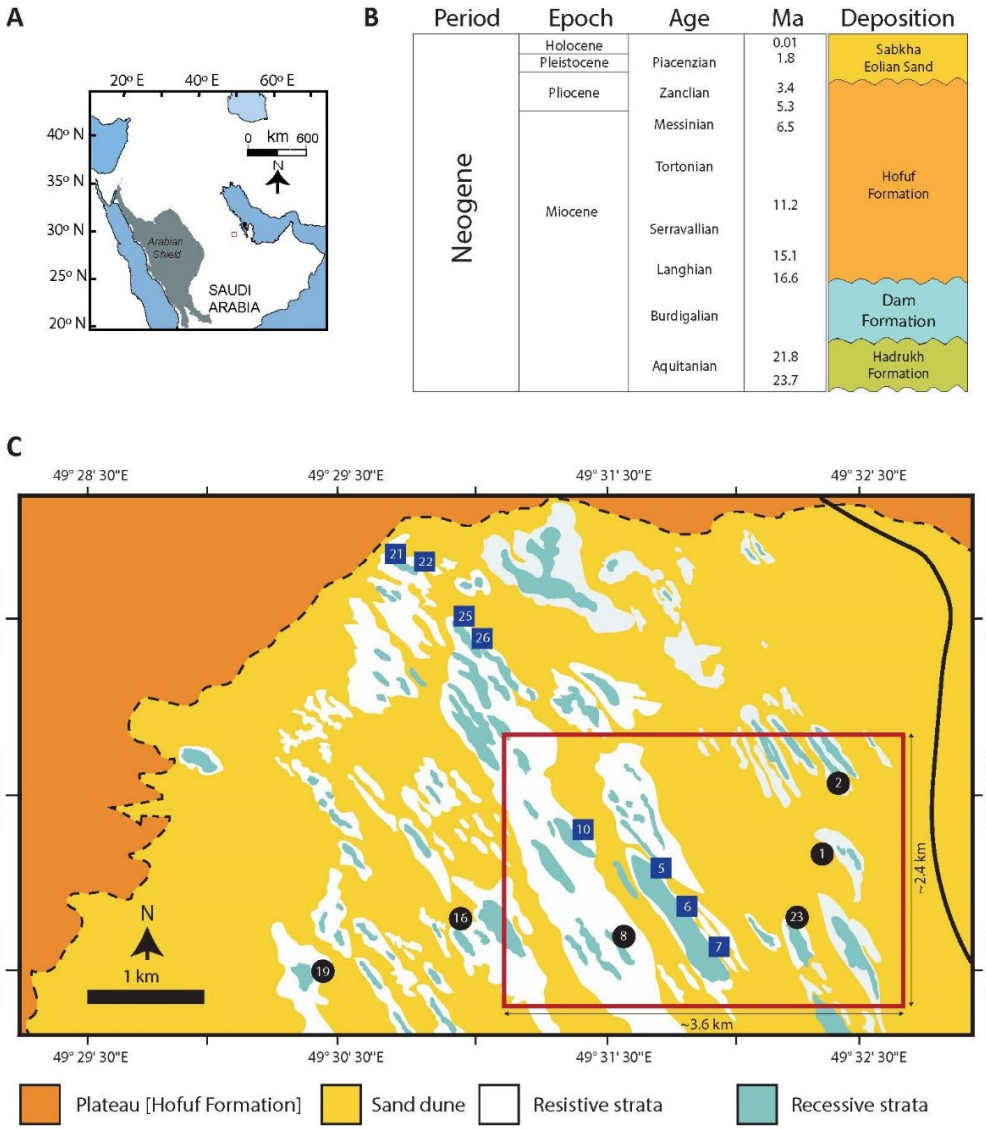

Fig. 1: Stratigraphy of the Dam Formation and the study area in the Lidam area in eastern Saudi Arabia: (A) map of the study area in eastern Saudi Arabia; (B) stratigraphic column showing that the Dam Formation overlies the Hadrukh Formation and is overlain by the Hofuf Formation (modified from Powers et al., 1966); (C) Geological map of the Lidam area showing outcrops of the uppermost part of the the Dam Formation. Note that the outcrop numbered with blue box trend ~ NW - SE parallel to the presumable paleo shoreline (studied by Ali, 2015). The outcrop numbered with black circles trend approximately E-W, perpendicular to the presumable paleo shoreline, (studied by Bashari et al. 2017). The red box indicates the area of interest (AOI) where the 3D modeling was perfromed.

Preprints (www.preprints.org) | NOT PEER-REVIEWED | Posted: 16 September 2020 doi:10.20944/preprints202009.0366.v1

The first transect (Fig. 1C) includes six measured sections and represents a trend that runs approximately E-W, presumably perpendicular to the paleo shoreline of the environment of depositions (Bashri et al., 2017). The second transect (Fig. 1C) includes eight measured sections and represents a trend that runs approximately NW-SE, presumably parallel to the paleo shoreline of the environment of depositions (Ali, 2015). For the 3D geostatistical modeling, we selected a location that surrounded eight outcrops from these studied outcrops (Fig. 1C). The location that was selected was found to have one side with approximately 2.40 km in the N-S direction and another side with approximately 3.64 km in the E-W direction (Fig. 1C). This location was enclosed by a rectangular polygon that had an area of 8.73 km^2. In the subsequent discussion, we will refer to this polygon as an area of interest (AOI).

3.2. Stratigraphy

Data from the measured sections in the study area include details about stratigraphic units and the sequence stratigraphic framework, which were presented as 2D cross-sections (Fig. 2) by Ali (2015) and Bashri et al. (2017). The stratigraphic surfaces, such as sequence boundaries and maximum flooding surfaces (Fig. 2), were used in this study to construct surfaces and constrain the zones in the 3D geostatistical models. Parasequences, bed sets, and bed thickness were used to define the layers in the 3D geostatistical models.

3.3. Lithology

The data from the measured sections in the study area include detailed lithological descriptions (Table 1). Although there were slight differences in the lithological descriptions provided by Ali (2015) and Bashri et al. (2017), particularly in the naming and grouping of the facies, the differences were not substantial, and the lithological skim of the study area from these two studies can be unified. Based on grain type, texture and size, sedimentary structure, fossil content, and

Preprints (www.preprints.org) | NOT PEER-REVIEWED | Posted: 16 September 2020 doi:10.20944/preprints202009.0366.v1

stratigraphic pattern, Ali (2015) identified 17 lithofacies, whereas Bashri et al. (2017) identified 15 lithofacies (Table 1). These lithofacies were grouped in lithofacies associations and used as input for modeling the facies (Table 1; see section 4.2).

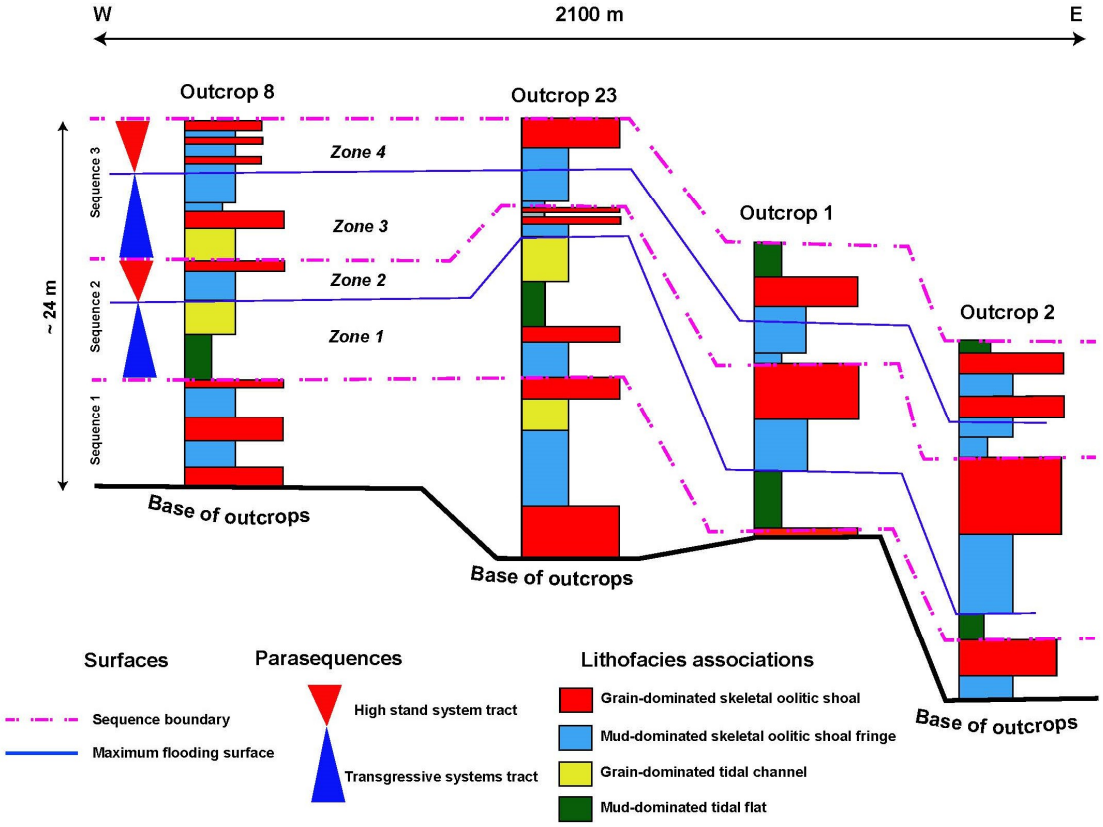

Fig. 2: Sequence stratigraphic model of the Dam Formation in the Lidam area (modified from Bashari et al. 2017).

3.4. Petrophysics

Data from the measured sections in the study area include the results of 105 paired porosity and permeability measurements conducted on core plugs with diameters of 1.5 inches (Abdelkarim et al., 2019). The data of porosity and permeability were integrated with the lithofacies data and used to generate 3D porosity and permeability models, which were used for mapping permeability anisotropy and running the flow simulation conducted in this study.

Preprints (www.preprints.org) | NOT PEER-REVIEWED | Posted: 16 September 2020 doi:10.20944/preprints202009.0366.v1

3.5. Conceptual model

The data from the measured sections include conceptual models for the Dam Formation in the study area (Alkhaldi, 2009; Ali, 2015; Bashri et al., 2017; Abdelkarim et al., 2019). The conceptual model demonstrated that the Dam Formation in the Lidam area represents facies belts of tidal flat lithofacies associations crossed with tidal channels. The paleo shoreline of this conceptual model was interpreted to trend approximately NW-SE. These conceptual models were used to verify the final geostatistical model by comparing the output of the 3D facies model and the conceptual model in terms of the distribution of lithofacies belts.

4. Workflow

The workflow of this study was comprised of five steps, all of which were conducted in Petrel™ 2019). Step 1): Generate a 3D structural grid for the AOI to serve as a structural framework for the 3D facies and petrophysical models; Step 2): Generate the 3D facies models; Step 3): generate the 3D petrophysical models; Step 4): upscale the 3D grid and petrophysical properties; and Step 5): run the fluid flow simulation.

4.1. Generate the 3D structure grid

First, we constructed a 3D structural grid for the AOI (approximately 2.4 km by 3.64 km, i.e., an area of approximately 8.73 km^2) (Fig. 3A). The 3D grid was generated using a simple grid method since there no faults were found in the AOI. The location of the 3D grid was constrained by four geographic points, i.e., two latitude points (i.e., 25° 13' 55.65 and 25° 15' 15.20) and two longitude points (i.e., 49° 29' 52.15 and 49° 32' 4.66) (Fig. 3A). In the 2D horizontal dimension, the 3D grid had 86,400 cells, i.e., 240 cells in the side of the north-south direction and 360 cells in the side of the east-west direction (Fig. 3B). Each cell had the dimensions of 10 m x 10 m (Fig. 3B

Preprints (www.preprints.org) | NOT PEER-REVIEWED | Posted: 16 September 2020 doi:10.20944/preprints202009.0366.v1

4). These dimensions were designed to capture the lateral lithological heterogeneity of the tidal flat setting, and they were intended to generate a 3D facies model that is significantly finer than the subsurface models, which usually have cells that have the dimensions of 250 m x 250 m.

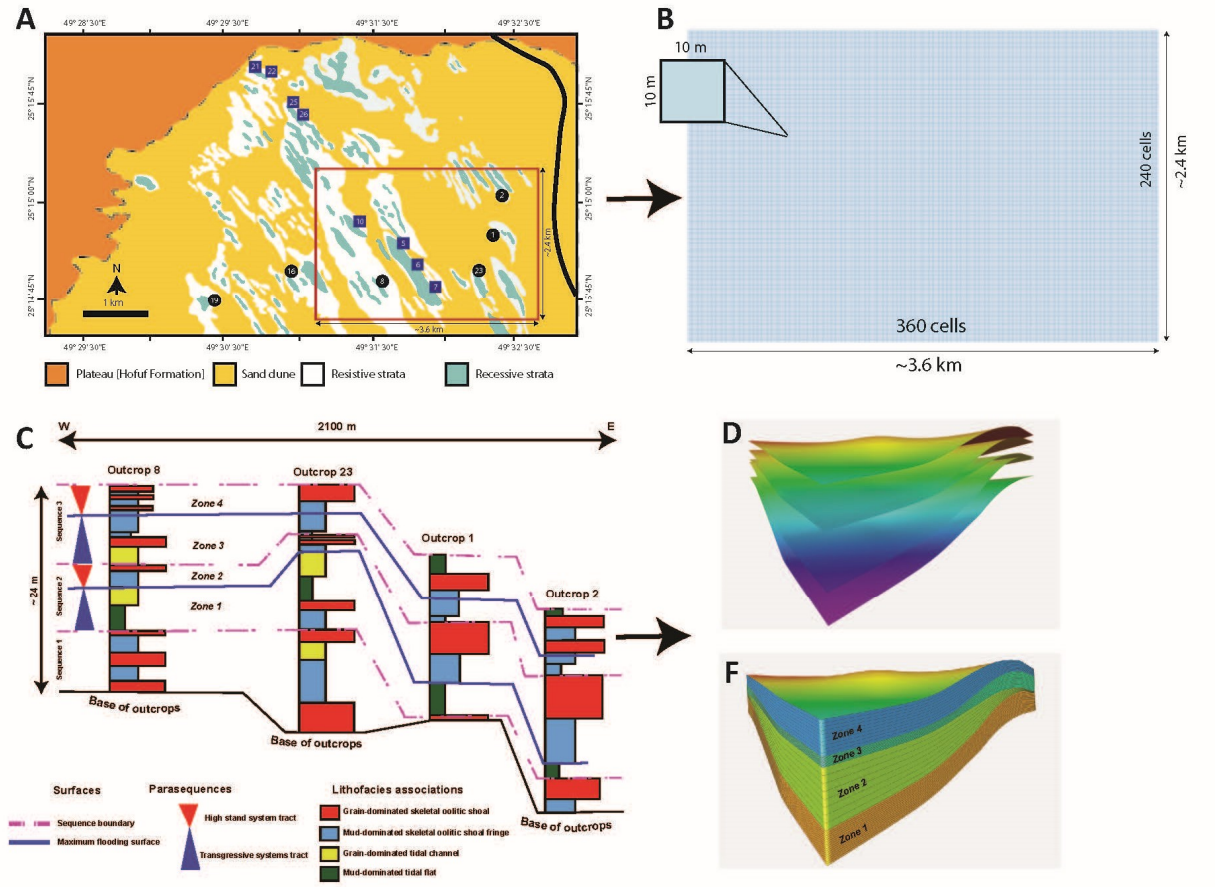

Fig. 3: Workflow to construct the grid, zones, and layers in the 3D model of the Dam Formation: (A and B) Gridding of the AOI. Note the cell size, which is 10 x 10 m; (B-E) Making surfaces and layers based on sequence stratigraphic framework of the Dam Formation at outcrop.

We used a stratigraphic framework from the previous studies to generate surfaces within the 3D grid that was constructed (Figs. 3C, 3D). Five stratigraphic intervals were defined from previous studies, and they were used to generate five surfaces in the 3D grid (Fig. 3D). These stratigraphic intervals are (from bottom to top): 1) the first sequence boundary (SB 1); 2) the first maximum flooding surface (MFS 1); 3) the second sequence boundary (SB 2); 4) the second

Preprints (www.preprints.org) | NOT PEER-REVIEWED | Posted: 16 September 2020 doi:10.20944/preprints202009.0366.v1

maximum flooding surface (MFS 2); and 5) the top of the outcrops (which we considered as the third sequence boundary [SB 3]). These five surfaces defined the four reservoir zones (zones 1 – 4) in the constructed model (Figs. 3C, 3D).

The layers in the reservoir zones that were constructed (Figs. 3E) determine the thickness of the cells in the 3D grid. These layers are considered as the main architectural elements in each zone, and they must adequately replicate the architecture of the stratigraphic units in the outcrop. Thus, layers within the constructed reservoir zones were assigned based on lithofacies thickness. The thickness of the layer in the 3D model was 0.2 m, and there were 65 layers in the model. After constructing these 65 layers, the total number of cells in the 3D grid was 360 x 240 x 65 cells, i.e., 5,616,000 cells.

4.2. Generate the 3D facies model

In 3D facies modeling, we populated the lithofacies that were defined by previous studies as discrete data into the 5,616,000 cells of the 3D grid. This step consisted of five tasks, i.e., 1) group and conceptualize the identified lithofacies of the studied outcrops (Figs. 4, 5A, 5B); 2) digitize the facies of the measured sections (Figs. 5C, 5D); 3) scale up the digitized lithofacies log to the cells of the 3D grid (Figs. 5C, 5D); 4) perform data analysis (Figs. 5E, 5F); and 5) distribute the upscaled facies data into the 5,616,000 cells of the 3D grid (Fig. 5G).

The first task is to group the lithofacies of the studied outcrop into genetically-related lithofacies associations (Table 1, Figs. 5A, 5B). The suggested lithofacies associations were (from offshore to onshore, Fig. 4): 1) the grain-dominated skeletal oolitic shoal; 2) the mud-dominated skeletal oolitic shoal fringe; 3) the mud-dominated tidal flat, and 4) the grain-dominated tidal channel.

Preprints (www.preprints.org) | NOT PEER-REVIEWED | Posted: 16 September 2020 doi:10.20944/preprints202009.0366.v1

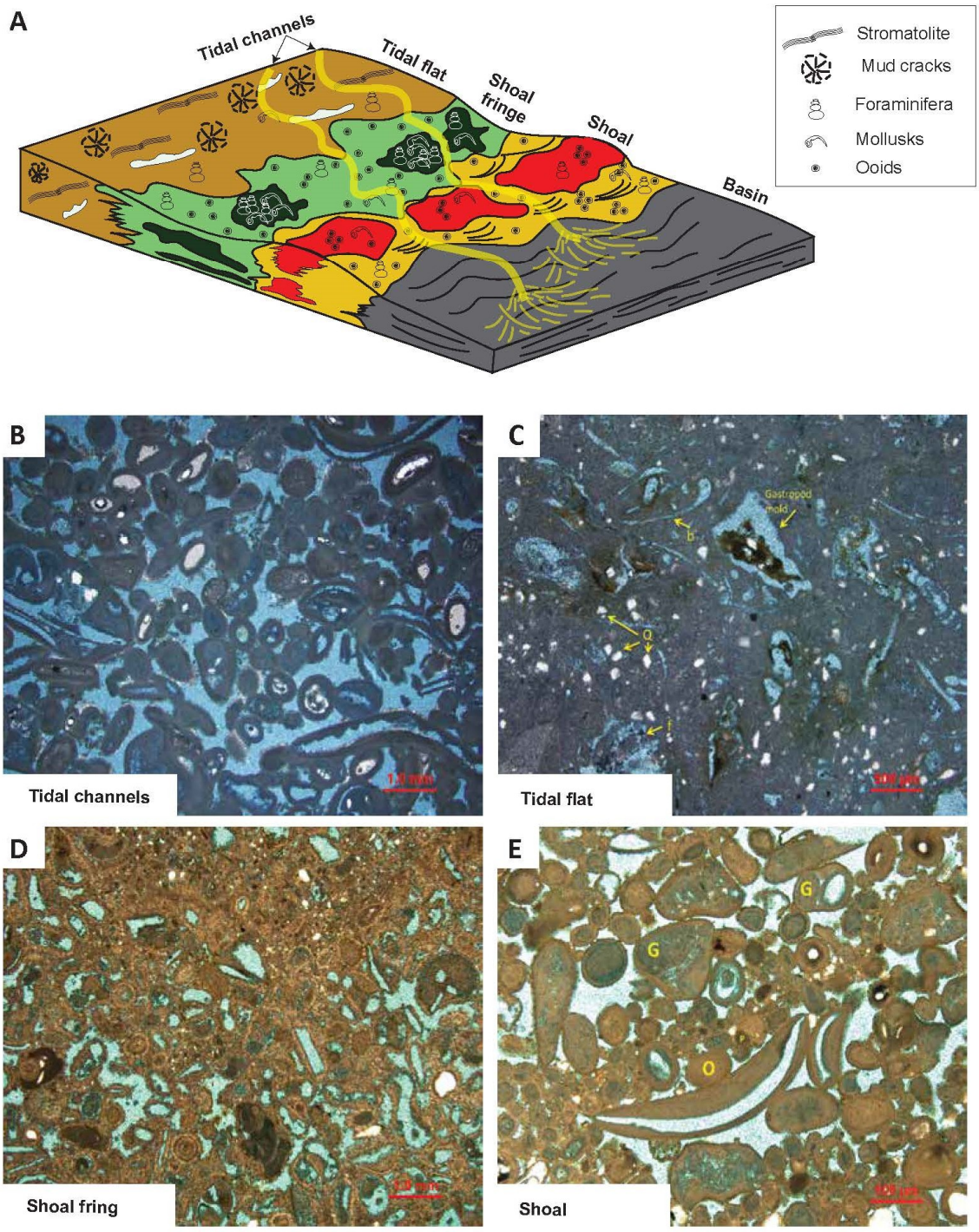

Fig. 4: (A) Conceptual model of the environment of deposition of the studied interval in the upper Dam Formation. Note that the model consists of two grain-dominated lithofacies association (B and E) and two mud-dominated lithofacies association (C and D).

Preprints (www.preprints.org) | NOT PEER-REVIEWED | Posted: 16 September 2020 doi:10.20944/preprints202009.0366.v1

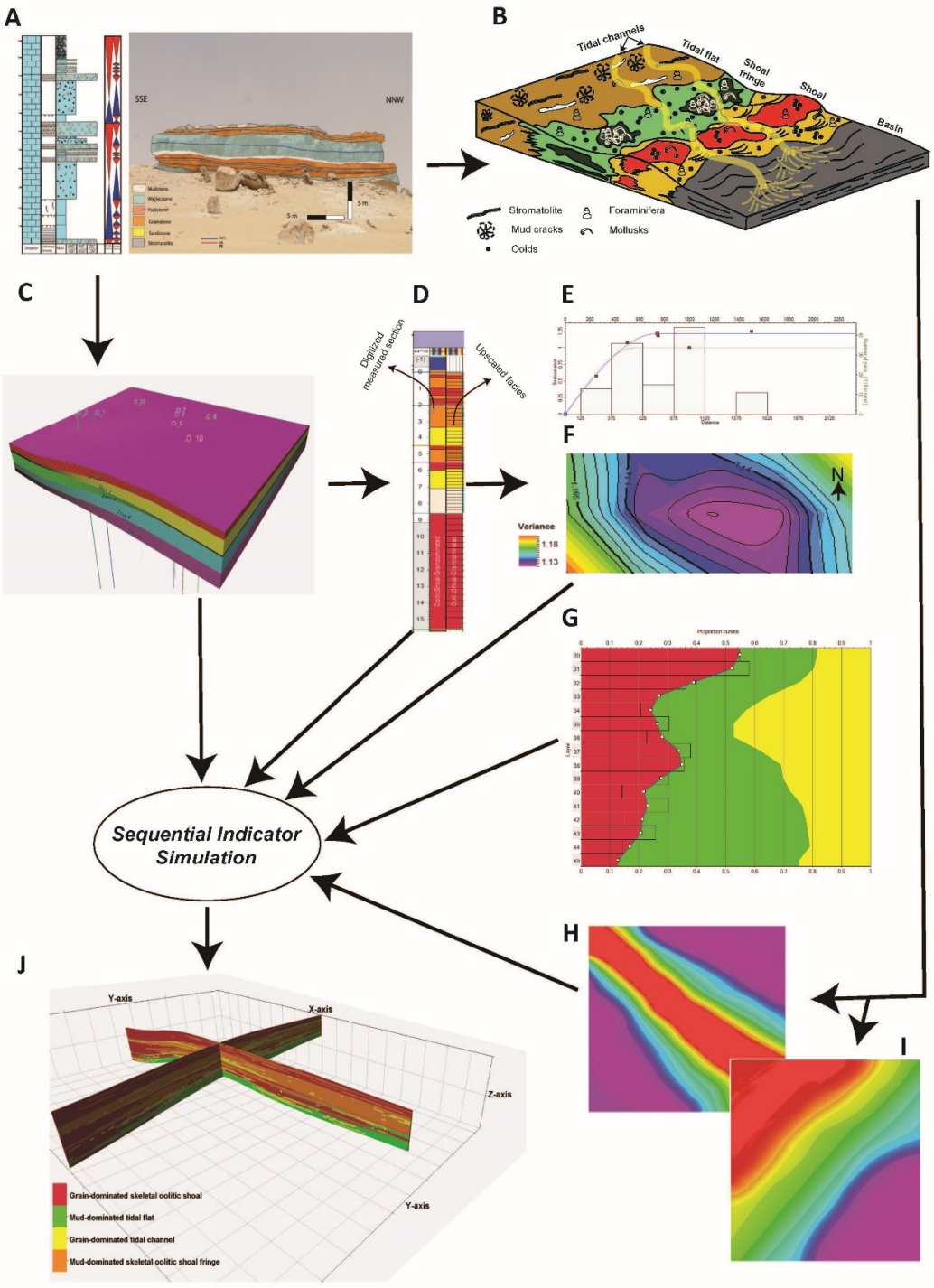

Fig. 5: Workflow to distribute facies in the 3D model of the Dam Formation. (A and B) grouping facies to lithofacies association; (C) structural grid; (D) Upscaling facies of the measured section to layers of the model; (E) experimental and modeled variograms; (F) Variogram map; (G) Lithofacies proportions; (H and I) Trend maps; (J) Two vertical slices in the resulting 3D facies model.

Preprints (www.preprints.org) | NOT PEER-REVIEWED | Posted: 16 September 2020 doi:10.20944/preprints202009.0366.v1

Table 1: Lithofacies and lithofacies association in the the Dam Formation (Bashari et al., 2017).

Lithofacies Association	Lithofacies	Texture	Grain types	Sedimentary structures
Mud-dominated tidal flat	Interbedded mudstone and evaporites	Mudstone and evaporites	–	Some lamination
	Interbedded cross-bedded sandstone and mudstone	Sandstone and mudstone	Quartz grains	Flaser bedding, tidal bundles and reactivation surfaces
	Stromatolites	Boundstone	–	Lamination
Grain-dominated tidal channels	Channelised medium sandstone	Sandstone	Quartz and skeletal grains	Herringbone cross-bedding
	Trough cross-bedded sandstone	Sandstone	Quartz grains	Trough cross-bedding
	Interbedded cross-bedded coarse limestone and mudstone	Grainstone and mudstone	Ooids and skeletal grains	Fenestrae vugs and tepee structure
	Intraformational limestone conglomerate	Grainstone	Mud clasts	–
	Planar cross-bedded skeletal peloidal grainstone	Grainstone	Skeletal and peloidal grains	Planar cross-bedding
Grain-dominated skeletal oolitic shoal	Herringbone cross-bedded skeletal oolitic grainstone	Grainstone	Ooids and skeletal grains	Herringbone cross bedding and keystone vugs
	Trough cross-bedded aggregate intraclast oolitic grainstones	Grainstone	Aggregate, intraclasts and ooids	Trough cross-bedding
	Massive peloidal skeletal packstone	Grainstone	Peloids and skeletal grains	–
	Channelised planar cross-bedded skeletal oolitic grainstone	Grainstone	Ooids, skeletons and grapestones	Planar cross-bedding
	Dipping planar-bedded skeletal oolitic grainstone	Grainstone	Ooids and skeletal grains	Planar bedding and lamination
Mud-dominated skeletal oolitic shoal fringe	Massive skeletal wackestone	Wackestone	Skeletal grains	–
	Massive quartz skeletal peloidal wacke-packstone	Wackestone–packstone	Quartz, skeletal and pellets	–

The second task is to digitize the lithofacies of the measured sections and insert them as facies logs in pseudo wells that represent the locations of the outcrops (Figs. 5C, 5D). The facies data of the measured sections in the AOI were digitized manually. Each lithofacies association was assigned a facies code (e.g., 1, 2, 3). Each one of these codes was given a certain stratigraphic interval based on the outcrop data. Thus, the facies log can be used as input data for 3D modeling.

The third task was to scale up the digitized facies log to the cells of the 3D grid (Figs. 5C, 5D). In this sense, each pseudo well includes 65 layers of different facies. The upscaled facies data (Fig. 6D) represented the hard data of the 3D model at the well location and were used for data analysis (Figs. 5E - 5G). The upscaled data were used to perform quality control of the modeling results in the sense that the resulting 3D facies model should honor the up-scaled data.

Preprints (www.preprints.org) | NOT PEER-REVIEWED | Posted: 16 September 2020 doi:10.20944/preprints202009.0366.v1

The fourth task was to perform the data analysis (Figs. 5E - 5G). The functionality of the analysis of the statistical data is determined by the discrete (indicator) variogram analysis (Fig. 5E), the variogram map (Fig. 5F), the proportion of the vertical facies (Fig. 5G), and the thickness of the facies. This functionality allowed us to check the quality of the input of data to understand statistical variations in the lithofacies. The results of the data analysis and the conceptual sedimentological model were used to construct a geologically-sensible, 3D facies model.

In the fifth task, we generated 2D trend maps (horizontal maps) using the proposed conceptual model for the Dam Formation in the study area (Figs. 5H, 5I). In this trend maps, the environment of depositions of the lithofacies associations (shoal; shoal fringe; tidal flat; tidal channel) were shaped to present the spatial arrangement of their geographic trends (Figs. 5H, 5I). These trend-maps determined the spatial probability of each lithofacies association.

In the final task of this step (task 6, Fig. 5J), the digitized lithofacies in the pseudo wells were distributed in the cells of the models using Sequential Indicator Simulation (SIS). The SIS function was constrained by the parameters of the variograms that were constructed in the data analysis step, and guided by the trend maps.

4.3. Generate 3D property model

Two important properties, i.e., porosity and permeability, were modeled in this study (Fig. 6). The values of porosity and permeability were taken from Abdelkarim et al. (2019) (Fig. 6C). Porosity and permeability were populated into the 5,616,000 cells of the 3D grid using a facies-based function in which the distribution of these properties was performed distinctly for each facies in the 3D facies model using the Gaussian random function simulation (GRFS) algorithm in Petrel™2019 (Figs. 6D, 6E). The data required to perform GRFS in Petrel™2019 were the range,

Preprints (www.preprints.org) | NOT PEER-REVIEWED | Posted: 16 September 2020 doi:10.20944/preprints202009.0366.v1

minimum, maximum, mean, and standard deviation values of the simulated porosity and permeability. These values were used to constrain the random distribution of porosity and permeability in each distinct lithofacies association throughout the 3D grid (Figs. 6F, 6G). Average porosity and permeability maps for each zone were generated to detect the overall trend of these properties in the zones. These types of maps are useful because they filter out the noise that results from the unrealistic distribution of facies (algorithm errors). Variogram maps of the average maps were generated to understand the permeability anisotropy of each reservoir zone in the 3D model.

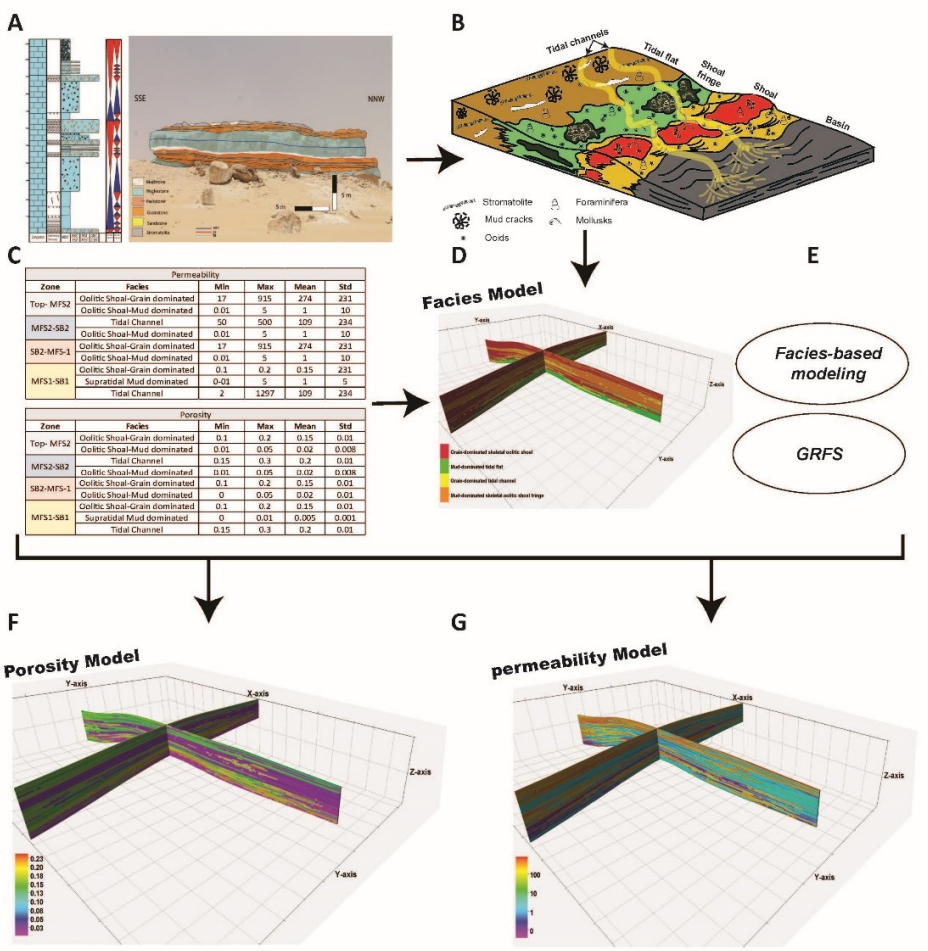

Fig. 6: Workflow to distribute porosity and permeability in the 3D model of the Dam Formation: (A and B) grouping facies to lithofacies association; (C) assigning porosity and permeability values to lithofacies association (data from a previous study by Abdulkareem et al., 2017); (D and E) distributing the porosity and permeability data in the 3D grid using the facies-based method; (E and F) Vertical slices of the porosity and permeability models

Preprints (www.preprints.org) | NOT PEER-REVIEWED | Posted: 16 September 2020 doi:10.20944/preprints202009.0366.v1

4.4. Generate upscaled models

In the upscaling process, we generated a coarser 3D grid model from the fine grid model, which had 5,616,000 cells. The upscaling process is essential to allow our current computer lab capacity to run flow simulation, which involved complicated mathematical algorithms on the generated models. We created coarser grid cells with a cell dimension of 100 m x 100 m (a grid with 23,125 cells). This coarser grid reduced the total number of cells from about 5,616,000 to 23,125 cells. The 3D property models of the fine grid cells (i.e., the 5,616,000-cell grid) were transferred to these coarser grids that were generated (23,125 cells). Although the number of cells was reduced substantially in the upscaled grid, this reduction did not considerably affect the petrophysical distribution in the 3D models.

4.5. Fluid flow simulation

The fluid flow simulation was run using the black-oil simulator (Eclipse 100) in Eclipse-Petrel™2019. The simulation was run on the upscaled model, which was assumed to be a heavy oil reservoir with impermeable sides and a cap as boundary conditions. The pressure support was assumed to come from a water aquifer below the oil-water contact. The production of the heavy oil from this hypothetical outcrop reservoir comes from vertical wells deployed to represent three transects.

The first transect (wells A1 - A3) and the second transect (wells A1, A4, A5) were designed to test the variation of oil production with permeability anisotropy in zone 1, along and across the tidal flat channel (first and second transects, respectively). Oil-water contacts for both transects were placed at the base of the tidal channel lithofacies. The perforation interval of the wells in both transects included the entire interval between the base of the channel and the upper boundary of zone 1 (MFS1). Thus, the production of oil was ensured to come from the tidal flat channels.

Preprints (www.preprints.org) | NOT PEER-REVIEWED | Posted: 16 September 2020 doi:10.20944/preprints202009.0366.v1

The third transect included four wells (B1 - B4) and was designed to test the variation of oil production with permeability anisotropy in zone 2. Oil-water contact for wells B1 -B4 was placed at the base of zone 2 (MFS 1). Perforation of these four wells included the entire interval in the zone. Thus, the production of oil was ensured to come only from the lithofacies in zone 2.

Nine fluid flow simulation runs were performed with the production of oil coming from only one single well from the three transects in each simulation run (one production well at a time). Each well in these three transects had the single control model of a production rate of 10,000 STB/day. The initial water saturation of the hypothetical reservoir of the outcrop was 0.5, whereas the preliminary heavy-oil formation-volume factor was 1.1. Water saturation and formation factors are dynamic parameters that continuously fluctuate with time, production, and changes in the pressure. The software considers these dynamic changes and adjusts these parameters through time. It should be noted that the fluid flow simulation was run only for zone 1 and 2 with the notion that the results of zone 1 would be similar to the result in zone 3 and the results of zone 2 would be similar to the result of zone 4 because of the similarity in lithofacies distribution and petrophysical data of these zones.

5. RESULTS

5.1. Analysis of the Data

Results of the data analysis (Fig. 5E - 5G) provide constraints on the vertical facies proportion, facies thickness, and facies probability of the 3D facies model. These constraints were computed from the upscaled lithofacies logs as vertical proportion curves and as percentages of the volume to the total model (Fig. 5E - 5G). The results of the data analysis also include experimental and modeled variogram parameters (nugget, sill, and major and minor ranges, Table 2), and variogram

Preprints (www.preprints.org) | NOT PEER-REVIEWED | Posted: 16 September 2020 doi:10.20944/preprints202009.0366.v1

maps (Fig. 5F). The results of the data analysis identified two different directions of the major range of the variograms. The major range for the grain-dominated skeletal oolitic shoal, the mud-dominated skeletal oolitic shoal fringe, and the mud-dominated tidal flat were found to be oriented approximately to NW-SE (Table 2). In contrast, the major range for the grain-dominated tidal channel was found to be oriented approximately to the ~NE-SW (Table 2). The minor range of the constructed variograms for all of these lithofacies associations was markedly lower than their corresponding major ranges (Table 2).

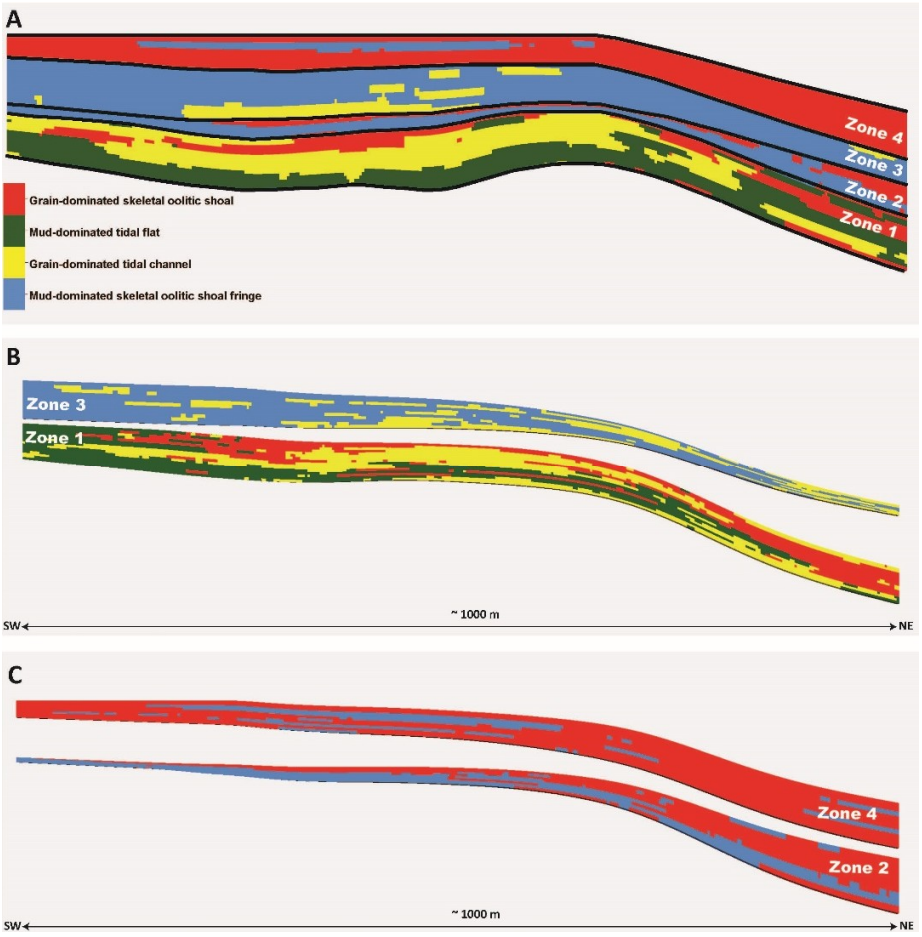

Fig. 7: Vertical slices from the 3D facies model showing: (A) the reservoir zones and lithofacies distribution in each zone, which is comparable to the distribution in the outcrop; (B) wedges of zones 1 and 3 (thickening land-ward, SW) and wedge of zones 2 and 4 (thickening basin-ward, NE).

Preprints (www.preprints.org) | NOT PEER-REVIEWED | Posted: 16 September 2020 doi:10.20944/preprints202009.0366.v1

Table 2: Variogram parameters of the lithofacies associations.

	variogram range (m)			variogram direction		variogram Sill
Lithofacies Association	**Major**	**Minor**	**Vertical**	**Major**	**Minor**	0.99
Mud-dominated tidal flat	2000	1000	0.4	NW-SE	NE-SW	0.99
Grain-dominated tidal channels	1200	500	1	NE-SW	NW-SE	0.99
Grain-dominated skeletal oolitic shoal	2000	1000	0.4	NW-SE	NE-SW	0.99
Mud-dominated skeletal oolitic shoal fringe	2000	1000	0.4	NW-SE	NE-SW	0.99

Table 3: Proportion of ithofacies associations in each reservoir zone in the 3D model.

	Lithofacies proportion (%)				
Lithofacies Association	**Entier 3D reservoir**	**Zone 1**	**Zone 2**	**Zone 3**	**Zone 4**
Mud-dominated tidal flat	38.4	42	0	0	0
Grain-dominated tidal channels	15	26.8	0	18.6	0
Grain-dominated skeletal oolitic shoal	14.3	31.2	48.2	0	81.5
Mud-dominated skeletal oolitic shoal fringe	32.3	0	51.8	81.4	18.5

5.2. Distribution of the lithofacies

Results showed both lateral and vertical variations in lithofacies of the 3D facies model (Fig. 7; Table 3). Each reservoir zone in the 3D facies model had a distinct set of lithofacies with a proportion comparable to the proportion of lithofacies in the outcrops of the study area (Fig. 7A). Zones 1 and 3 had extensive tidal channels (Fig. 8) that trended in the same direction suggested by the outcrop data (NE-SW). The average facies map of each zone in the 3D model (Fig. 9) smoothed the results of facies modeling and provided general trends of lithofacies in each zone. Whereas zones 1 and 3 (Figs. 9A, 9C) showed a general NE-SW trend, zones 2 and 4 (Figs. 9B, 9C) showed a NW-SE trend. Descriptions of the lithofacies in each reservoir zone are provided in the following sections.

Preprints (www.preprints.org) | NOT PEER-REVIEWED | Posted: 16 September 2020 doi:10.20944/preprints202009.0366.v1

5.2.1. Zone 1

Zone 1 (between SB 1 at the base and MFS1 on top) consisted of three lithofacies associations (Fig. 7A; Table 3), i.e., 1) a mud-dominated tidal flat (comprises the majority of the zone, ~42%); 2) grain-dominated tidal channels (comprise ~26.8% of the total volume of the zone); and 3) a grain-dominated skeletal oolitic shoal (comprises ~31.2% of the total volume of the zone). The grain-dominated tidal channel lithofacies association cluster as one channel volume that comprises ~21.9% of the total volume of lithofacies in the zone (Fig. 8). The long axis of this volume of the channel trends ~ NE-SW (Fig. 9A), and it cuts across the other two lithofacies associations in the zone, which are oriented NW-SE (Fig. 9A).

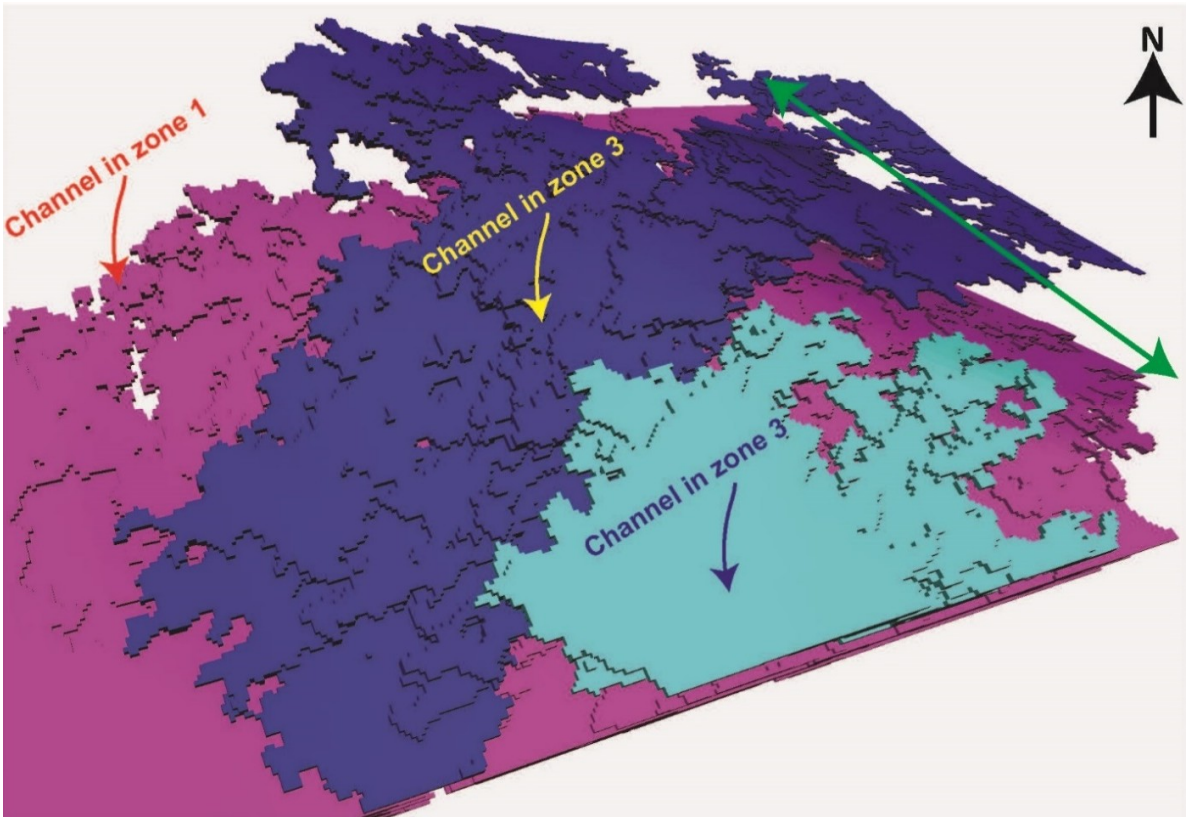

Fig. 8: Results of connectivity analysis of tidal channel lithofacies association showing the first three largest connected bodies of tidal flat channels in zones 1 and 3: Note that these bodies are elongated in the direction extended ~ NE-SW.

 doi:10.20944/preprints202009.0366.v1

5.2.2. Zone 2

Zone 2 (between MFS 1 at the base and SB 2 on top) consists of two lithofacies associations (Fig. 7C; Table 3), i.e., 1) the mud-dominated skeletal oolitic shoal fringe (comprises the majority of the zone, 51.8%) and 2) the grain-dominated skeletal oolitic shoal (comprises 48.2% of the total volume of the zone). Unlike the zones above and below, the grain-dominated tidal channel lithofacies are absent in this zone (Fig. 9). The grain-dominated skeletal oolitic shoal represents the downdip lithofacies for the mud-dominated skeletal oolitic shoal fringe (Fig. 9B), and, in a few areas, the grain-dominated skeletal oolitic shoal is surrounded by the mud-dominated skeletal oolitic shoal fringe (Fig. 9B).

5.2.3. Zone 3

Zone 3 (between SB 2 at the base and MFS 2 on top) consists of two lithofacies associations (Fig. 7A; Table 3): 1) grain-dominated tidal channel (comprises 18.6% of the total volume of the zone); and 2) mud-dominated skeletal oolitic shoal fringe (comprises the majority of the zone, 81.4%). In this zone, the grain-dominated tidal channel trend NE-SW (Figs. 8, 9) forms ~15.2% of the total volume of lithofacies in this zone. Although visually look like isolated bodies in the average map of the zone (Fig. 9C), tidal channels show high connectivity (Fig. 8). Out of the 15.2% volume of the tidal channel, 12% accumulates in on connected volume (Fig. 8).

5.2.4. Zone 4

Zone 4 (between MFS 2 at the base and the top of the outcrops) consists predominantly of grain-dominated oolitic shoal (which comprises 81.5% of the total volume of the zone) (Fig. 7; Table 3). There are patches of the mud-dominated skeletal oolitic shoal fringe (comprises the majority of the zone, 18.5%), which occur as elongated bodies and tend to be parallel to the

Preprints (www.preprints.org) | NOT PEER-REVIEWED | Posted: 16 September 2020 doi:10.20944/preprints202009.0366.v1

shoreline (Fig. 9D). The grain-dominated tidal channel lithofacies also are absent in this zone (Fig. 9).

5.3. Architecture of the Lithofacies

Previous works on the Dam Formation resulted in the construction of shoreline-controlled sequence stratigraphy with the suggestion that the paleo shoreline of the Dam Formation has a strike direction that trends approximately NW-SE. The 3D model of the facies in this study showed architectures of the lithofacies that were comparable to those suggested by the sequence stratigraphic framework of the Dam Formation in the previous studies (Fig. 7). Therefore, the internal architecture of the 3D facies model can be classified into transgressive and regressive parasequences.

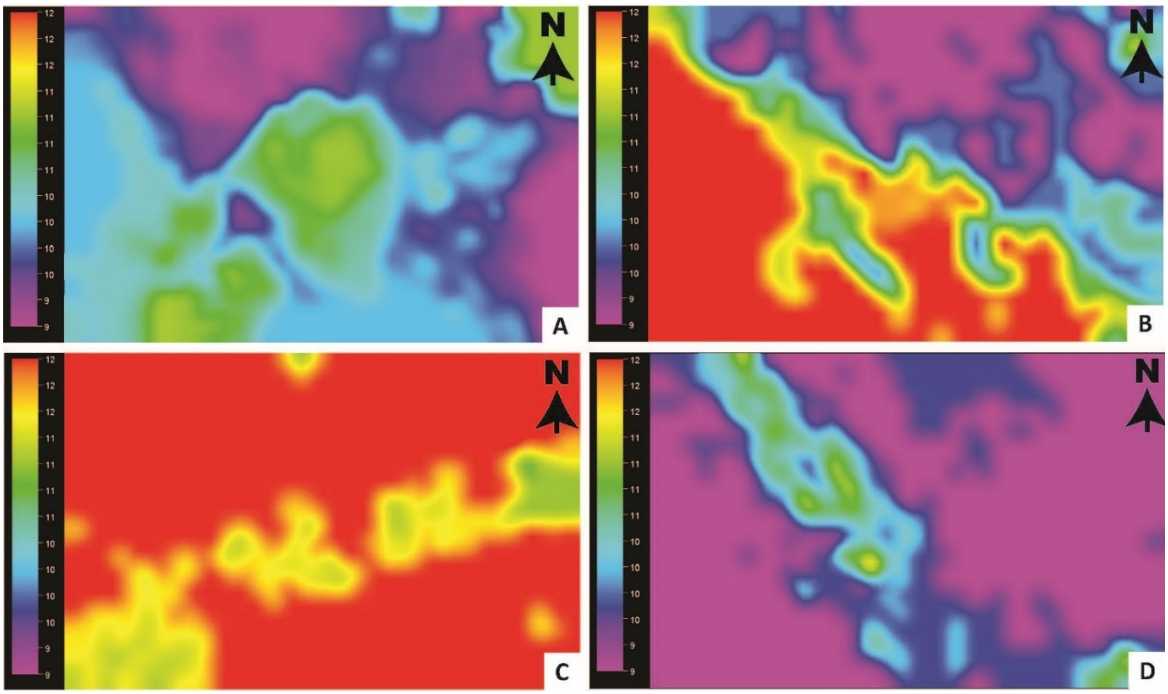

Fig. 9: Average maps of lithofacies associations in the four zones of the 3D facies model: Note the spatial relationship between the suggested pale shoreline (trends NW-SE) and the lithofacies in each zone. Zones dominated by grain-dominated tidal flat lithofacies association (Zones 1, 3) have trends perpendicular to the suggested pale shoreline, whereas zones dominated by grain-dominated shoal lithofacies associations (Zones 2, 4) have trends parallel to the suggested pale shoreline.

 doi:10.20944/preprints202009.0366.v1

Zones 1 and 2 comprise sequence 2 of the Dam Formation (Fig. 2). The basal part of zone 1 (Fig. 7) is a mud-dominated tidal flat, and the grain-dominated tidal channel lithofacies associations, which occur as transgressive facies, were retrograded on top of SB 1 (Fig. 7). The occurrence of these lithofacies associations in zone 1 is consistent with the early transgressive parasequences of Bashari et al. (2017). The grain-dominated oolitic shoal occupies the upper part of zone 1 (Fig. 7) and occurs extensively proximal to the proposed shoreline as late transgressive parasequences that are consistent with Bashari et al. (2017) sequence stratigraphic model. Zone 2, which overlies the MFS 1 (Fig. 7), is dominated by the extensive, grain-dominated, skeletal oolitic shoal, which reflects the suggested high-stand system tract of sequence 1. Remarkably, in zone 2, the grain-dominated tidal channel lithofacies are absent, suggesting shoreline transgression and retrogradation of the shoal lithofacies in the direction of the land.

Zones 3 and 4 comprise sequence 3 of the Dam Formation (Fig. 2). The mud-dominated tidal channel lithofacies association with bodies of tidal flat channel in zone 3 is interpreted to represent the transgressive parasequences of sequence 3 (Fig. 7). However, the extensive grain-dominated skeletal oolitic shoal of zone 4 is interpreted to represent the regressive part of sequence 3. This interpretation is consistent with the sequence stratigraphic framework of the Dam Formation proposed by Bashari (2015).

The 3D facies model revealed some similarities in trends and distribution of the facies between zones 1 and 3 (Fig. 7B) and between zones 2 and 4 (Fig. 7C). This similarity can be linked to the above-defined sequence stratigraphic framework of the 3D model. Both zones 1 and 3 (Fig. 7B) represent the transgressive facies of sequences 2 and 3, respectively, which are referred to in the following discussion as zones with TF. Zones 2 and 4 (Fig. 7C), on the other hand, represent the regressive facies of these sequences, respectively (these zones are referred to in the following

Preprints (www.preprints.org) | NOT PEER-REVIEWED | Posted: 16 September 2020 doi:10.20944/preprints202009.0366.v1

discussion as zones with RF). The zones with TF have wedges that are thickening to the SW and thinning to the NE (Fig. 7B). In contrast, the layers in the zones with RF have a wedge shape with the opposite trend, i.e, they thicken to the NE and become thinner to the SW (Fig. 7C).

5.4. Trends in petrophysical properties

The 3D models of porosity and permeability have a coherent match with the facies distribution and architecture, showing consistent vertical and lateral correspondence (Fig. 10). Unsurprisingly, the grain-dominated lithofacies associations have better porosity and permeability values than the mud-dominated lithofacies association (Fig. 10). The porosity and permeability values of the zones with TF (zones 1 and 3) appear to be influenced by the presence of the grain-dominated tidal channels lithofacies association (Fig. 10). The average maps of porosity and permeability of zones with TF (zones 1 and 3) (Fig. 11) showed relatively high values of porosity (ranging from approximately 15% to 20%) and permeability (ranging from approximately 100 to 200 mD) compared to other values in the background lithofacies (which range from 5% to 10% and from 2 to 20 mD for porosity and permeability, respectively). These relatively higher values organize in trends that are consistent with the channel body trends (~NE-SW) (Fig. 11). Generally, the porosity and permeability have the highest values at the center of these channel bodies (~20 and ~200 mD, respectively) and decrease to the flank of the channel body (~15 and ~100 mD, respectively) (Fig. 11). The variogram map of permeability in zone 1 indicated an elliptical shape with NE-SW direction in the variance value and indicated that geometric anisotropy occurred perpendicular to the proposed shoreline for the environment of depositions (Fig. 12A). In zone 3, such a trend is not well-defined (Fig. 12C).

In contrast to the zones with RF, average maps in zones with RF have areas with porosity and permeability trending NW-SE, and they are arranged in a parallel manner (Fig. 13). These maps

Preprints (www.preprints.org) | NOT PEER-REVIEWED | Posted: 16 September 2020 doi:10.20944/preprints202009.0366.v1

(Fig. 13) showed a contrast between areas of a relatively higher porosity and permeability (ranging from 10% to 15% and from 150 to 300 mD, respectively) and areas with a relatively lower permeability (ranging from 2% to 5% and from 2 to 25 mD, respectively) (Fig. 13). Generally, the porosity and permeability values have intermediate values at the transitions areas between these contrasting areas (Fig. 13). The variogram map of permeability in zones 2 and 4 (zones with RF) showed an elliptical shape in the NW-SE direction for the variance value, indicating that geometric anisotropy occurs parallel to the proposed shoreline for the environment of depositions (Figs. 12B, 12D).

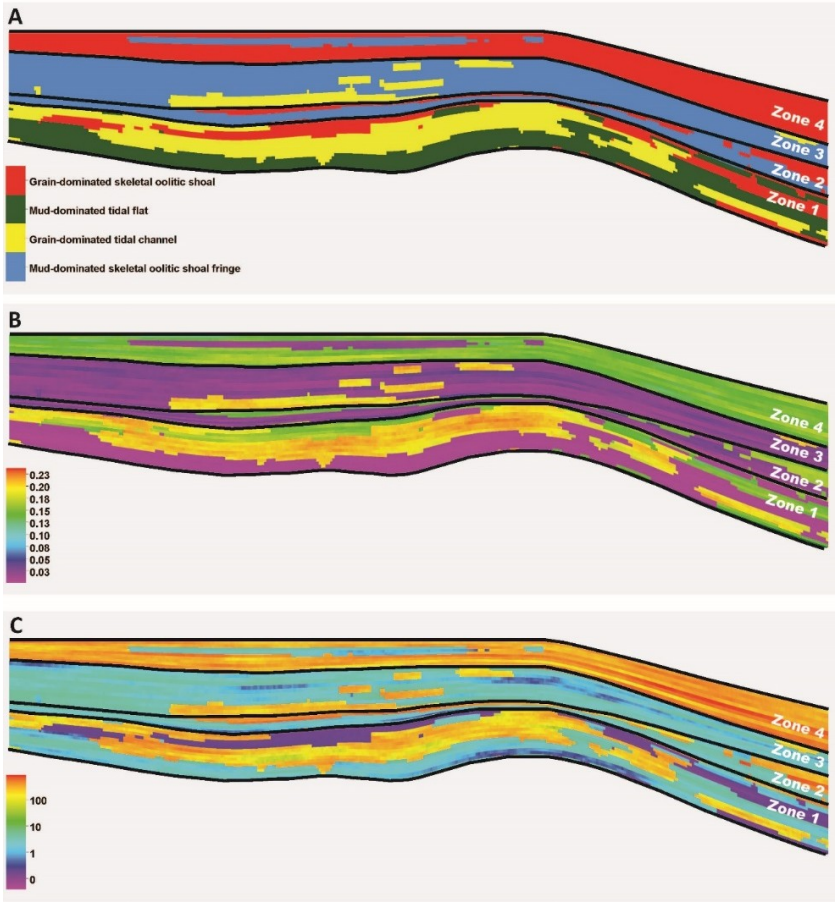

Fig. 10: Vertical slices: (A) in the 3D facies, (B) in the 3D porosity, and (C) in the 3D permeability models. Note that the models of porosity and permeability have a coherent match with the facies distribution and architecture.

Preprints (www.preprints.org) | NOT PEER-REVIEWED | Posted: 16 September 2020 doi:10.20944/preprints202009.0366.v1

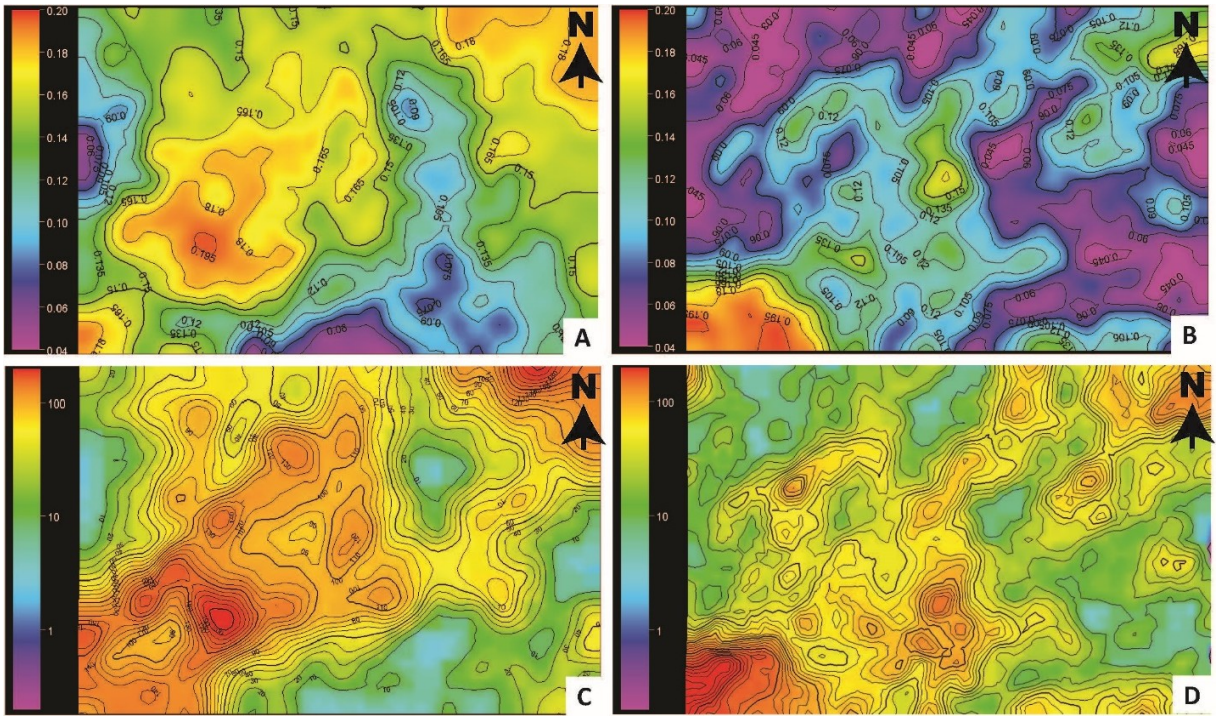

Fig. 11: (A and B) Average porosity maps and (C and D) average permeability maps for zones 1 and 3. Note that there are trends in high values of porosity and permeability to ~NE-SW consistent with the trend of the grain-dominated tidal channel lithofacies associations in these zones.

5.5. Trends in fluid flow behavior

In the simulation runs, we used three indicators for oil production that changed through the specified time for the simulation runs (Figs. 14-16), i.e., 1) oil in place (OIP); 2) oil production cumulative (OPC), and 3) oil recovery efficiency (ORE). In each of the three well transects, these indicators varied based on the location of the well. At each location of a well (i.e., before the production of oil in the static model), the permeability in the reservoir zone varied, whereas the OIP for the entire model stayed the same. Thus, the variation in production indicators can be attributed to the lateral variation in permeability (permeability anisotropy). The simulation time of all of the wells in the three transects was set to 80 years (Fig. 13B). At time zero, the OIP in the

Preprints (www.preprints.org) | NOT PEER-REVIEWED | Posted: 16 September 2020 doi:10.20944/preprints202009.0366.v1

model was the same for all of the wells, i.e., 32.85 x 10^6 STB, and started to degrees through time with the production of oil (Figs. 13-15).

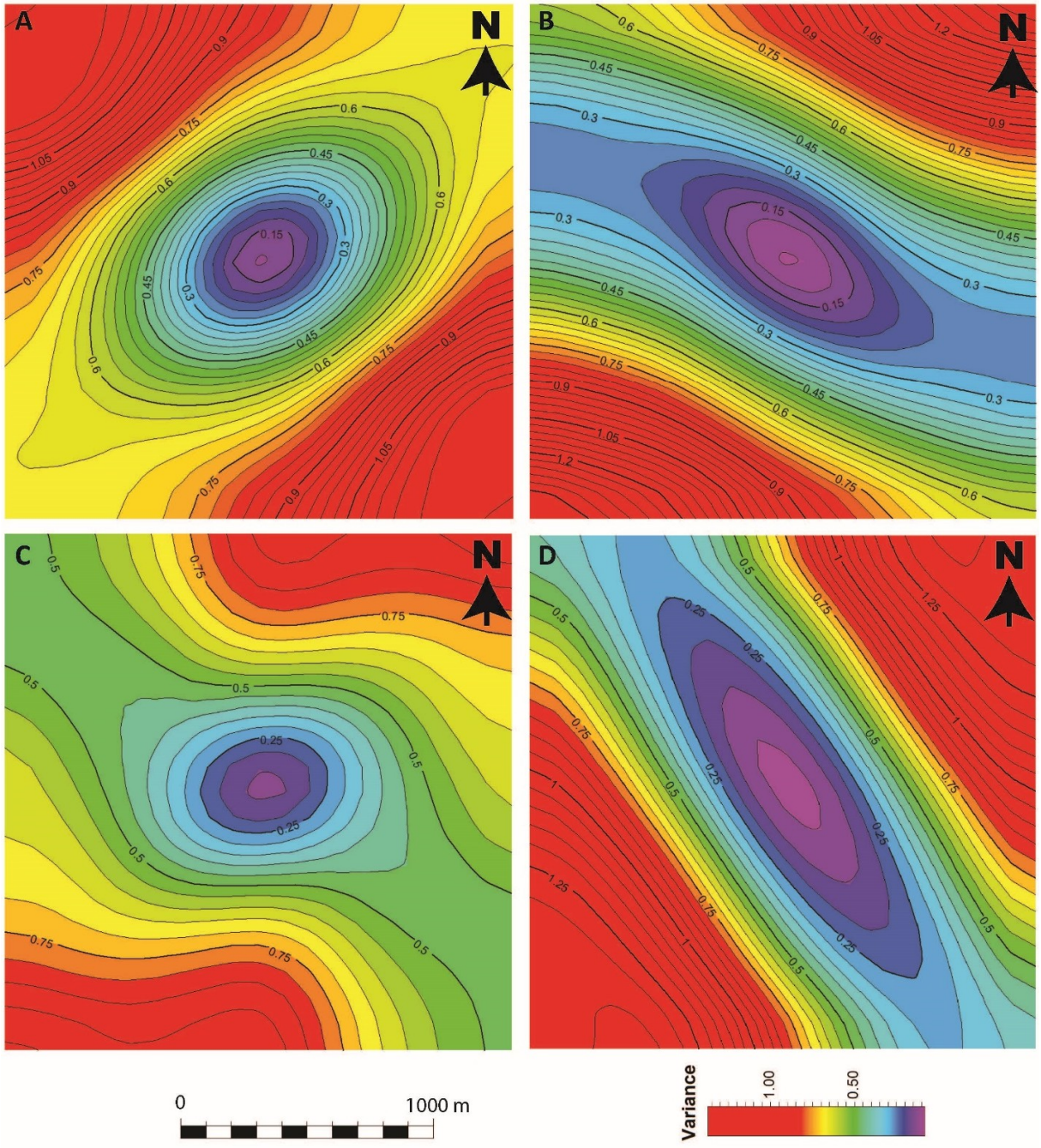

Fig. 12: Variogram maps of the permeability values in each of the average maps of the reservoir zones in the 3D model: (A) zone 1; (B) zone 2; (C) zone 3; (D) zone 4. Note that these variograms show elliptical shapes with the major direction markedly longer than the minor range, suggesting geometric permeability anisotropy.

Preprints (www.preprints.org) | NOT PEER-REVIEWED | Posted: 16 September 2020 doi:10.20944/preprints202009.0366.v1

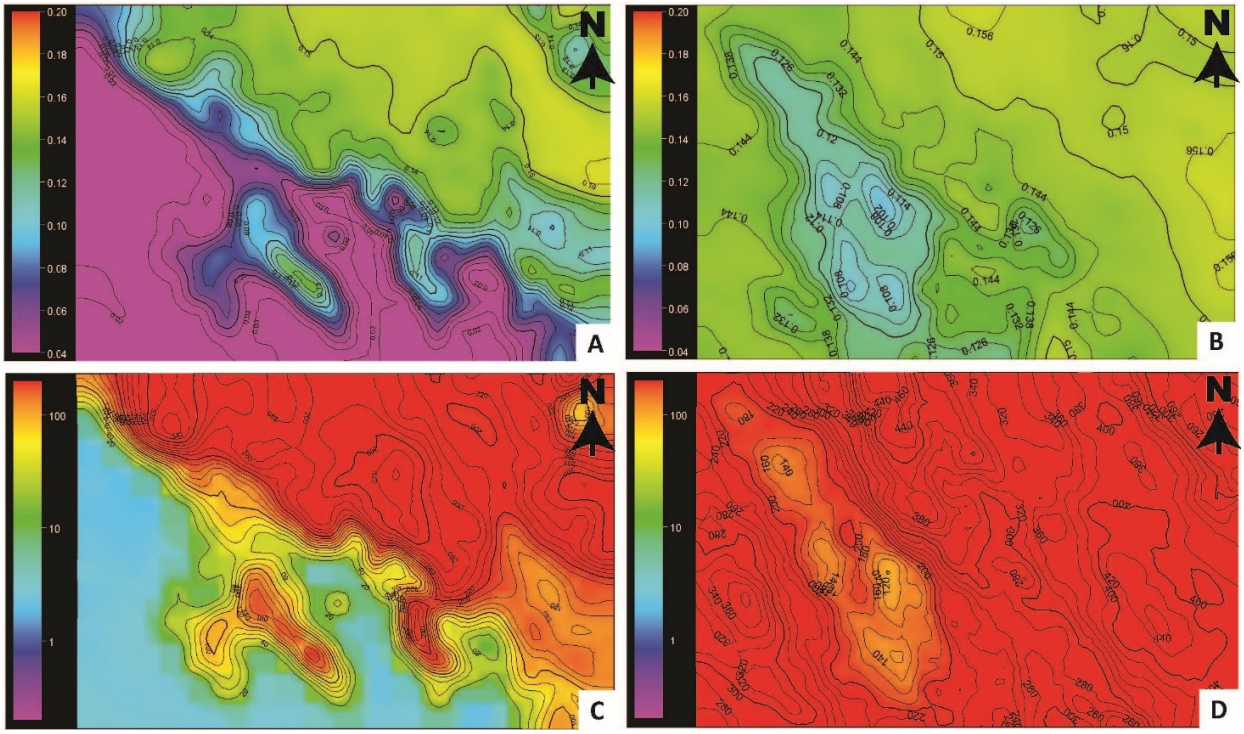

Fig. 13: (A and B) Average porosity maps and (C and D) average permeability maps for zones 2 and 4. Note that there are trends in high values of porosity and permeability to ~NW - SE consistent with the trend of the grain-dominated oolitic shoal lithofacies associations in these zones.

5.5.1. First transect

The first transect (Wells A 1-3, Fig. 14A) has an updip-downdip trend perpendicular to the interpreted shoreline of the environment of depositions of the Dam Formation. This transect was designed to test the variation in the production of oil along the axis of the tidal flat channel. In the simulation, the following results were indicated after 20 years:

- Well A 1, which was located in the updip direction (Fig. 14A) showed the highest ORE (0.2) (Fig. 14C) with an OPC of 6.9 x 10^6 (STB) (Fig. 14B) and a decrease in OIP to 25.9 x 10^6 (STB) (Fig. 14A);
- Well A 2, which fell between Wells A 1 and A 2 (Fig. 14A) had an ORE of 0.1 (Fig. 14C), an OPC of 2.2 x 10^6 (STB) (Fig. 14B), and a decrease in OIP to 25.9 x 10^6 (STB) (Fig. 14A);

Preprints (www.preprints.org) | NOT PEER-REVIEWED | Posted: 16 September 2020 doi:10.20944/preprints202009.0366.v1

- Well A 1, which was located in the downdip direcion (Fig. 14A), had the lowest ORE (0.0005) (Fig. 14C), an OPC of 0.004 x 10^6 (STB) (Fig. 14B), and an insignificant decrease in OIP to ~32.79 x 10^6 (STB) (Fig. 13A).

5.5.2. Second transect

The second transect (Wells A1, A 4, and A 5, Fig. 15A) had a trend approximately parallel to the interpreted shoreline of the environment of depositions of the Dam Formation. This transect was designed to test the variation in oil production across the axis of the tidal flat channel in zone 1. In the simulation, after 20 years:

- Well A 1, which represented the central axis of the channel (Fig. 15A), had the highest ORE (0.2) (Fig. 15C) with an OPC of 6.9 x 10^6 (STB) (Fig. 15B) and a decrease in OIP to 25.9 x 10^6 (STB) (Fig. 15A);
- Wells A 4 and A 5, which represent production from the flank of the channel, showed markedly lower production indicators, i.e., ORE values of 0.04 and 0.006, respectively; OPC values of 1.5 x 10^6 (STB) and 0.21 x 10^6 (STB), respectively; and OIP values of 31.2 x 10^6 and 32.6 x 10^6, respectively [Fig. 15]).

5.5.3. Third transect

The thired transect (Wells B 1- 4) had a trend approximately perpendicular to the interpreted shoreline of the environment of depositions of the Dam Formation. This transact was designed to test the variation in oil production across the lithofacies associations in zone 2. After 20 years, the four wells in this transact showed the following trends in the simulation:

Preprints (www.preprints.org) | NOT PEER-REVIEWED | Posted: 16 September 2020 doi:10.20944/preprints202009.0366.v1

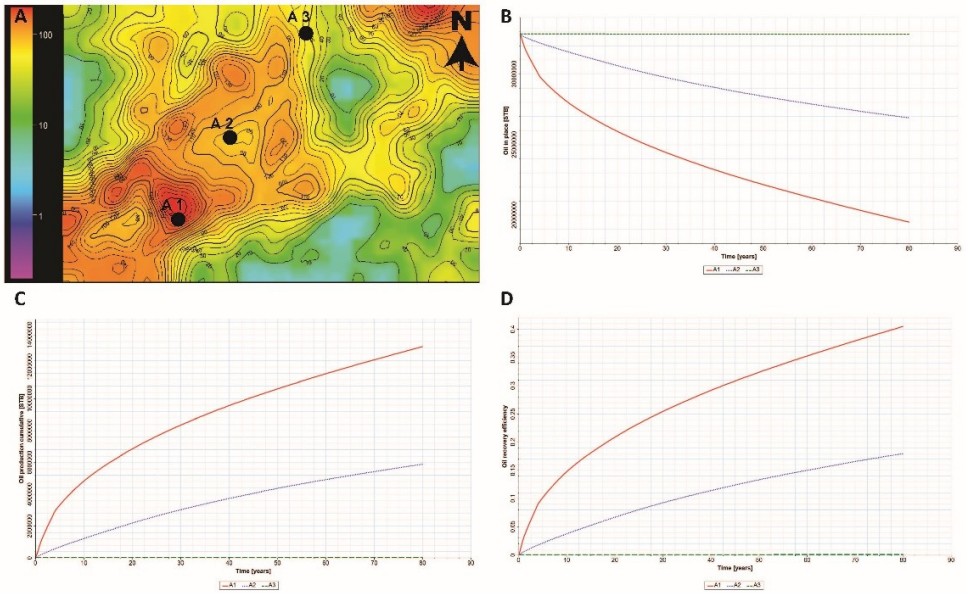

Fig. 14: (A) Average permeability map of zone 1 showing the spatial variation of permeability consistent with the tidal channel trend and also showing the locations of Well A 1 to 3 along the channel belt. (B-D) Results of fluid flow simulation including (B) oil in place (OIP); (C) oil production cumulative (OPC); and (D) oil recovery efficiency (ORE). Note that these production indicators suggest that the production of oil increased in the landward direction (SW).

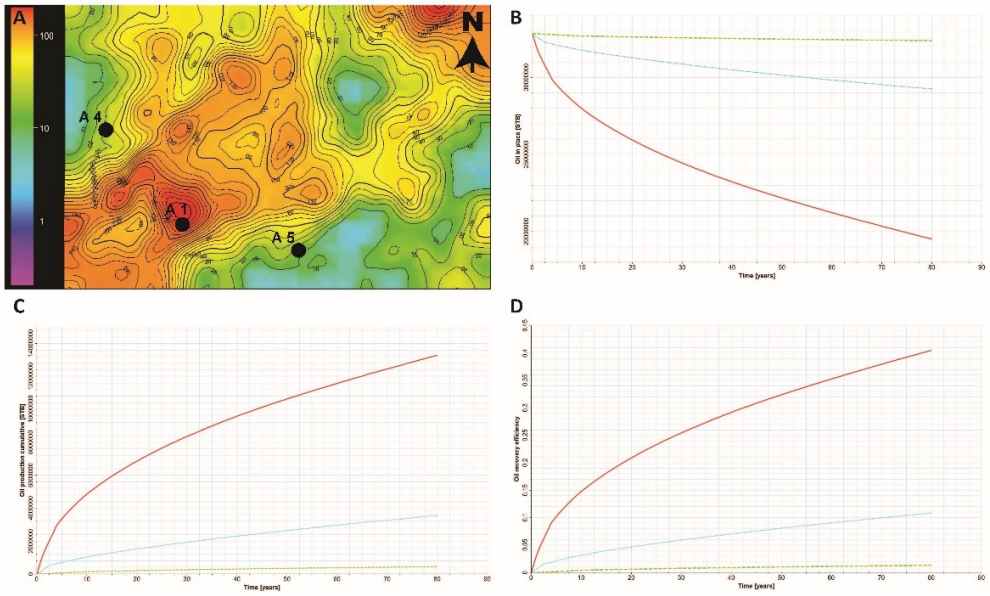

Fig. 15: (A) Average permeability map of zone 1 showing the spatial variation of permeability consistent with the tidal channel trend and aalso showing the locations of Wells A 1, 4, and 5 across the channel belt. (B-D) Results of fluid flow simulation including (B) oil in place (OIP); (C) oil production cumulative (OPC), and (D) oil recovery efficiency (ORE). Note that these production indicators suggest that oil production increased at the channel axis and decreased at the channel flank.

Preprints (www.preprints.org) | NOT PEER-REVIEWED | Posted: 16 September 2020 doi:10.20944/preprints202009.0366.v1

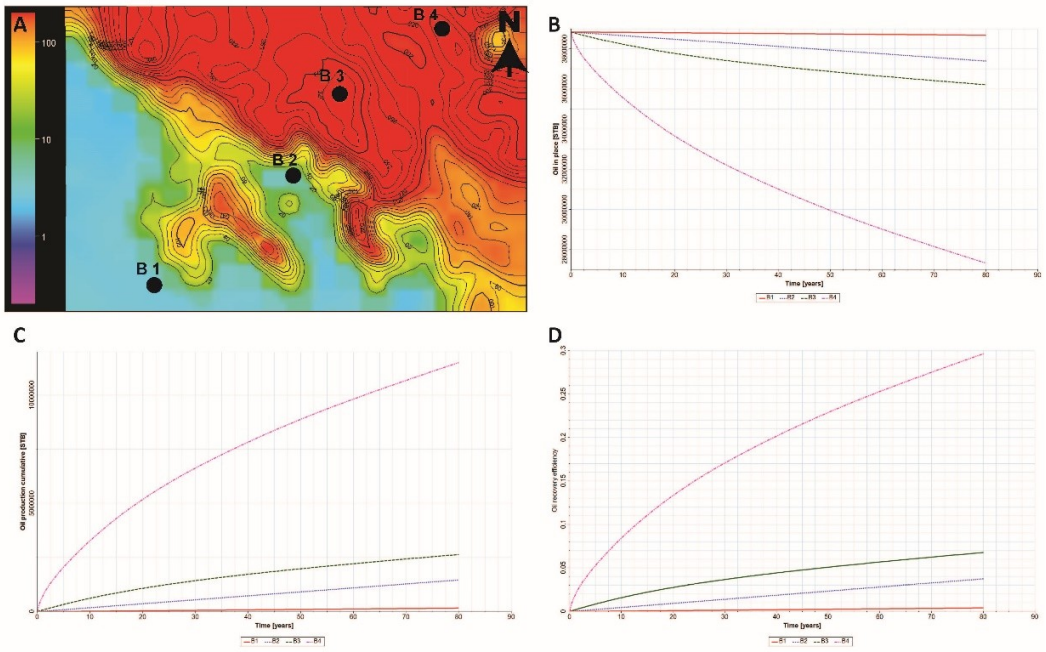

Fig. 16: (A) Average permeability map of zone 2 shows spatial variation of permeability consistent with the shoal lithofacies trend and also shows the locations of Well B 1 - 4 perpendicular to the shoal lithofacies. (B-D) Results of fluid flow simulation including (B) oil in place (OIP); (C) oil production cumulative (OPC), and (D) oil recovery efficiency (ORE). Note that these production indicators suggest that oil production increased to the SW. Note that these production indicators suggested that oil production increased in the direction of the basin (NE).

- ORE and OPC increase from the updip direction to the downdip direction (ORE is 0.1, 0.02, 0.009, and 0.001, and OPC is 5.1 x 106, 1.0 x 106, 0.36 x 106, and 0.04 x 106 (STB) for Wells B 1 - B 4, respectively [Figs. 15B, 16C]).
- OIP decreased from the updip direction to the downdip direction (OIP was 33.6 x 106, 37.7 x 106, 38.4 x 106, and 38.8 x 106 (STB) for Wells B 1 - B 4, respectively [Fig. 16D]).

6. Discussion

The results of the 3D geostatistical modeling made it possible to recognize trends and patterns in the spatial variability of the sedimentary strata and the petrophysical properties of the Dam Formation within a sequence stratigraphic framework. These results showed sedimentological, stratigraphic, and petrophysical patterns similar to the Dam Formation at the outcrop and similar

 doi:10.20944/preprints202009.0366.v1

to the modern analogs of tidal flat settings in different locations worldwide. The results of the fluid flow simulation suggested trends in the production of oil that were consistent with the trend in the anisotropy of permeability. Most importantly, these recognized trends and patterns in the results can be described quantitatively. Therefore, the resulting quantitative data can be utilized extensively as an analog to provide a robust assessment of permeability anisotropy and reservoir quality of strata deposited as tidal flat carbonate elsewhere.

6.1. Similarity of the 3D model to the modern analog and stratigraphic record

Both the conceptual (Fig. 4) and the 3D facies model (Fig. 7) in this study showed a grain-dominated, skeletal, oolitic shoal surrounded by a mud-dominated, skeletal oolitic shoal fringe that was cross-cut by tidal channels and flanked on the onshore side by the mud-dominated tidal flat lithofacies association. Interestingly, a similar arrangement of this pattern of lithofacies occurs in the modern analogs (Jung and Aigner, 2012; Purkis et al., 2015; Harris et al., 2016). For example, the documented lateral facies patterns observed in the Little Bahama Bank in northern Bahamas showed shoal facies surrounded by a mud-dominated background similar to what the 3D facies model has produced (Figs. 4, 7) (Rankey et al., 2004; Reeder et al., 2009; Harris et al., 2011). This is especially significant given that the Bahamas have different carbonate physiography than the Dam Formation, i.e., an isolated platform (Rankey et al., 2004; Reeder et al., 2009; Harris et al., 2011) versus a carbonate ramp (Cantrel et al., 2014). The 3D facies models also seem to be consistent with the modern facies pattern of the offshore UAE (Fig. 7) in that the grain-dominated skeletal oolitic shoal is surrounded by a fringe of mud-dominated skeletal oolitic shoals (Jung and Aigner, 2012).

The main difference between the stratigraphic record and the modern analogs of tidal flat settings is that the modern analogs represent one “snapshot” of the distribution of facies over time,

 doi:10.20944/preprints202009.0366.v1

whereas the stratigraphic record provides spatial and temporal perspectives for the distribution of facies (Jung and Aigner, 2012). Comparing the results of the 3D models (Fig. 7) with a stratigraphic record of a tidal flat in the Dam Formation suggests that the 3D models successfully reproduced the pattern of the tidal flat lithofacies association. This similarity between the 3D model and the modern analog and stratigraphic record of the tidal flat suggests that we constructed a 3D model that can represent the setting of a tidal flat that ultimately can be used to investigate the controls on permeability anisotropy.

6.2. Understanding permeability anisotropy using variogram parameters

The results of the 3D modeling suggested that permeability anisotropy of the tidal flat settings in the study area can be understood from the variogram parameters. The results showed that the variograms of the permeability in the four zones have elliptical shapes with a major range substantially longer than the minor range, which suggests geometric anisotropy (Fig. 12).

Previous modeling results of the Dam Formation in the Lidam area (Abdulkareem et al., 2017) showed similar results, i.e., the ranges of the variograms of the petrophysical properties have a major range that is remarkably longer than the minor ranges. However, it is important to note that the major and minor ranges of the variograms determined in this study (Table 1), i.e., approximately 2 km and approximately 1 km, respectively, are considerably longer than the ranges of the variograms reported by Abdulkareem et al. (2000), i.e., about 0.1 km and 0.03 km, respectively. This difference could be attributed to the limited area that was modeled by Abdulkareem et al. (2000), who modeled an area that measured approximately 0.23 km by 0.06 km, i.e., approximately 0.014 km^2, using measured sections that were closely-spaced, which means that a full representation of the spatial extent of the lithofacies was not available. Another possibility could be the fact that, in this study, we modeled lithofacies associations by grouping

 doi:10.20944/preprints202009.0366.v1

many individual lithofacies, whereas Abdulkareem et al. (2000) separately modeled the variograms of these lithofacies. In either of these two cases, the pattern of the variograms suggests geometric anisotropy for the lithofacies that were modeled, which resulted in permeability anisotropy, which can be explained in a sequence stratigraphic framework and by sea-level change.

6.3. Understanding permeability anisotropy with sequence stratigraphic framework

The results suggested that changes in the sea level could be the first-order control of permeability anisotropy in tidal flat settings. Zones with TF (zones 1 and 3) (Fig. 7) represent deposition at the time of decreases in the sea level. In such cases, permeability anisotropy is controlled by the tidal channels (Figs. 9 - 12). These channels usually flow perpendicular to the shoreline of the marine depositional environments (Figs. 9 - 12). In this case, high permeability areas concentrate around the channel belts, and low permeability areas concentrate away from the channel belts (Fig. 11). In the zones with RF (Figs. 9, 13), which represent deposition at the time of high-stand of the sea level, permeability anisotropy controlled by location with respect to the oolitic shoal lithofacies associations, which were arranged parallel to the shoreline of the marine environments (Fig. 13). In this case, areas with high permeability will be concentrated more toward the downdip and around areas occupied by shoal deposits (Fig. 13).

6.4. Predicting permeability anisotropy using production data and sequence stratigraphy

The hydrocarbon reserve of the presumable oil reservoir in the constructed 3D model is a function of the total porosity in each zone (Figs. 14 - 16). However, oil production of this presumable reservoir is a function of the permeability in the 3D model (Figs. 14 - 16). Since the production in each simulation run comes from a single well (Figs. 14 - 16), the oil reserves would not be affected by the location of the well in the model. In contrast, oil production indicators (i.e.,

 doi:10.20944/preprints202009.0366.v1

OIP, COP, and RF) through time (which is a function of permeability) are affected significantly by the location of the well in the model because of the permeability anisotropy (Figs. 14 - 16).

Results from fluid flow simulation showed that oil production indicators (OIP, COP, and RF) of wells that penetrate zone 1 increase closer to the tidal channel axis and in the up-dip direction and decrease at the flank of the channel belt and in the down-dip direction (Figs. 14, 15). The tidal flat channel lithofacies association on top of the sequence boundaries usually occurred extensively in the updip direction and narrowed down in the down-dip direction of the shoreline of the depositional environments (Fig. 7). This lithofacies association also has a wedge with a thick interval in the up-dip and a thin interval in the down-dip (Fig. 7). The flank of these channels usually are associated with mud-dominated lithofacies, resulting in poorer permeability than the axis of the channel (Fig. 11). Thus, it is most likely to encounter better reservoir quality rocks at the axis of the tidal channel lithofacies in the updip direction in strata representing transgressive parasequences of tidal flat setting (Figs. 14, 15).

In contrast to the oil production trend in zone 1, oil production indicators (OIP, COP, and RF) of wells that penetrate zone 2 increase basin-ward, i.e., in the downdip direction (Fig. 16). The association of the oolitic shoal lithofacies on top of a maximum flooding surface (Fig. 7) usually occurs extensively in the downdip direction, and it is pinched out in the updip direction of the depositional environments of the shoreline (Fig. 13). This lithofacies association also has a wedge with a thick interval in the downdip direction and a thin interval in the updip direction (Fig. 7). Thus, it is most likely to encounter better quality reservoir rocks associated with oolitic shoal lithofacies in the downdip direction in strata representing regressive parasequences of the tidal flat setting (Figs. 13, 16).

 doi:10.20944/preprints202009.0366.v1

6.5. Implications and limitations

This study provides interesting implications when integrating sequence stratigraphy with facies modeling, petrophysical modeling, and fluid flow simulation to understand permeability anisotropy in sequence stratigraphic framwork. The results provide insights into several aspects of the heterogeneity of lithofacies as well as petrophysical variations and reservoir connectivity in tidal flat lithofacies. Ultimately, the results offer quantitative data on how permeability anisotropy varies in tidal flat settings and how the variations affect the production of hydrocarbons. This information is useful in predicting areas for future drilling in carbonate reservoirs with tidal flat lithofacies.

It should be noted that, however, this study did not take into account the impact of the diagenesis of the petrophysical properties of reservoirs. Rather, the study considered mainly the variation in the depositional texture of lithofacies. This could be one limitation when using the results of the modeled outcrop to understand the equivalent subsurface reservoirs. It would be interesting if data of diagenesis in the the Dam Formation from the subsurface were integrated with the results of this outcrop study.

7. Conclusions

The 3D outcrop modeling (facies and property modeling) and the fluid flow simulation of tidal flat strata in the Dam Formation (in eastern Saudi Arabia) resulted in the following key findings:

1- In the 3D models, porosity and permeability vary vertically and laterally with the variation in lithofacies associations, suggesting depositional controls on permeability anisotropy of the studied tidal flat strata.

2- Fluid flow simulation results suggested that hydrocarbon production is influenced significantly by permeability anisotropy.

3- The 3D models and the results of the fluid flow simulation identified patterns and trends in permeability anisotropy and hydrocarbon production that could be linked to sequence stratigraphic framework.

Quantitatively, this study shows that permeability anisotropy in carbonate reservoirs of tidal flat settings is controlled significantly by trends in depositional environments (shoal trend versus tidal channel trend). In the stratigraphic record, such trends are predictable in sequence stratigraphic framework. Therefore, permeability anisotropy also could be predictable on sequence stratigraphic framework.

References

Abdelkarim, A.A., Abdullatif, O.M., Babalola, L.O., Makkawi, M.H., Yassin, M.A., 2019. High-resolution lithofacies and porosity modeling of the mixed siliciclastic–carbonate deposits of the Burdigalian Dam Formation, Eastern Saudi Arabia. Int. J. Earth Sci. https://doi.org/10.1007/s00531-018-1647-1

Ali, S., 2015. High-resolution stratigraphic architecture and sedimentological heterogeneity within the miocene dam formation, Eastern Province, eastern Saudi Arabia. King Fahd University of Petroleum and Minerals.

Alkhaldi, F., 2009. Controls on Hierarchy of Miocene Buildups within a High Resolution Cycle Stratigraphic Framework of Dam Formation, Lidam Area, Saudi Arabia. MSc thesis. King Fahd University of Petroleum and Minerals.

Amour, F., Mutti, M., Christ, N., Immenhauser, A., Tomás, S., 2011. Outcrop Analogue for a Mixed Siliciclastic-Carbonate Ramp Reservoir : A Multi-Scale Facies Modeling Approach, in: AAPG International Conference and Exhibition. AAPG, Milan, Italy.

Bashri, M., Abdullatif, O., Salih, M., 2017. Sedimentology and facies analysis of Miocene mixed siliciclastic–carbonate deposits of the Dam Formation in Al Lidam area, eastern Saudi Arabia. Arab. J. Geosci. https://doi.org/10.1007/s12517-017-3244-1

Branets, L. V, Ghai, S.S., Lyons, S.L., Wu, X.H., 2009. Challenges and technologies in reservoir modeling. Commun. Comput. Phys. https://doi.org/10.4208/cicp.2009.v6.p1

Cantrel, D.L., Nicholson, P., Hughes, G., Miller, M., Bhullar, A.G., Abdelbagi, S.T., Norton, A.K., 2014. Tethyan Petroleum Systems of Saudi Arabia, in: Memoir 106: Petroleum Systems of the Tethyan Region. https://doi.org/10.1306/13431867m1063615

Eltom, H., Makkawi, M., Abdullatif, O., Alramadan, K., 2013. High-resolution facies and porosity models of the upper Jurassic Arab-D carbonate reservoir using an outcrop analogue, central Saudi Arabia. Arab. J. Geosci. 6, 4323–4335. https://doi.org/10.1007/s12517-012-0708-1

Grover, G., Read, J., 1978. Fenestral and Associated Vadose Diagenetic Fabrics of Tidal Flat Carbonates, Middle Ordovician New Market Limestone, Southwestern Virginia. SEPM J. Sediment. Res. 48. https://doi.org/10.1306/212f74aa-2b24-11d7-8648000102c1865d

Harris, A.D., Covault, J.A., Madof, A.S., Tao, S.U.N., Sylvester, Z., Granjeon, D., 2016. Three-dimensional numerical modeling of eustatic control on continental-margin sand distribution. J. Sediment. Res. 86, 1434–1443. https://doi.org/10.2110/jsr.2016.85

Harris, P.M., Purkis, S.J., Ellis, J., 2011. Analyzing spatial patterns in modern carbonate sand bodies from Great Bahama Bank. J. Sediment. Res. https://doi.org/10.2110/jsr.2011.21

Iriem, O., 1987. Miocene tidal flat stromatolites of the Dam Formation, Sandi Arabia. Arab. J. Sci. Eng. 12, 145–153.

Jung, A., Aigner, T., 2012. Carbonate geobodies: Hierarchical classification and database - a new workflow for 3D reservoir modelling. J. Pet. Geol. 35, 49–65. https://doi.org/10.1111/j.1747-5457.2012.00518.x

Meyer, F.O., Price, R.C., Al-Ghamdi, I.A., Al-Goba, I.M., Al-Raimi, S.M., Cole, J.C., 1996. Sequential stratigraphy of outcropping strata equivalent to Arab-D reservoir, Wadi Nisah, Saudi Arabia. GeoArabia 1, 435–456.

Palermo, D., Aigner, T., Nardon, S., Blendinger, W., 2010. Three-dimensional facies modeling of carbonate sand bodies: Outcrop analog study in an epicontinental basin (Triassic, southwest Germany). Am. Assoc. Pet. Geol. Bull. 94, 475–512. https://doi.org/10.1306/08180908168

Petrovic, A., Aigner, T., Pontiggia, M., 2018. FACIES HETEROGENEITIES IN A RAMP CARBONATE RESERVOIR ANALOGUE: A NEW HIGH-RESOLUTION APPROACH FOR 3D FACIES MODELLING. J. Pet. Geol. 41, 155–174. https://doi.org/10.1111/jpg.12698

Pickup, G.E., Ringrose, P.S., Corbett, P.W.M., Jensen, J.L., Sorbie, K.S., 1995. Geology, geometry and effective flow. Pet. Geosci. 1, 37–42. https://doi.org/10.1144/petgeo.1.1.37

Powers, R., Ramirez, L., Redmond, C., Elberg, E., 1966. Geology of the Arabian peninsula. Geol.

Surv. Prof. Pap. 560, 1–147.

Pratt, B.R., JAMES, N.P., 1986. The St George Group (Lower Ordovician) of western Newfoundland: tidal flat island model for carbonate sedimentation in shallow epeiric seas. Sedimentology 33, 313–343. https://doi.org/10.1111/j.1365-3091.1986.tb00540.x

Purkis, S.J., Rowlands, G.P., Kerr, J.M., 2015. Unravelling the influence of water depth and wave energy on the facies diversity of shelf carbonates. Sedimentology 62, 541–565. https://doi.org/10.1111/sed.12110

Purkis, S.J., Vlaswinkel, B., 2012. Visualizing lateral anisotropy in modern carbonates. Am. Assoc. Pet. Geol. Bull. 96, 1665–1685. https://doi.org/10.1306/02211211173

Rankey, E.C., 2002. Spatial patterns of sediment accumulation on a holocene carbonate tidal flat, northwest Andros Island, Bahamas. J. Sediment. Res. 72, 591–601. https://doi.org/10.1306/020702720591

Rankey, E.C., Enos, P., Steffen, K., Druke, D., 2004. Lack of impact of Hurricane Michelle on tidal flats, Andros Island, Bahamas: Integrated remote sensing and field observations. J. Sediment. Res. https://doi.org/10.1306/021704740654

Rankey, E.C., Goodner, H., Doveton, J., 2018. Depositional architecture and petrophysical variability of an oolitic tidal sand shoal: Pennsylvanian (Missourian), Kansas, U.S.A. J. Sediment. Res. https://doi.org/10.2110/jsr.2018.57

Rankey, E.C., Morgan, J., 2002. Quantified rates of geomorphic change on a modern carbonate tidal flat, Bahamas. Geology 30, 583–586. https://doi.org/10.1130/0091-

7613(2002)030<0583:QROGCO>2.0.CO;2

Read, J.F., Grotzinger, J.P., Bova, J.A., Koerschner, W.F., 1986. Models for generation of carbonate cycles. Geology 14, 107–110. https://doi.org/10.1130/0091-7613(1986)14<107:MFGOCC>2.0.CO;2

Reeder, S.L., Rankey, E.C., Swart, P., 2009. A Tale of Two Storms: An Integrated Field, Remote Sensing and Modelling Study Examining the Impact of Hurricanes Frances and Jeanne on Carbonate Systems, Bahamas, in: Perspectives in Carbonate Geology. International Association of Sedimentologists, pp. 75–90. https://doi.org/10.1002/9781444312065.ch6

Shinn, E. a, 1983. Tidal flat environment. Carbonate Depos. Environ.

Shinn, E., Lloyd, M., Ginsburg, R., 1969. Anatomy of a Modern Carbonate Tidal-flat, Andros Island, Bahamas. SEPM J. Sediment. Res. Vol. 39. https://doi.org/10.1306/74d71dcf-2b21-11d7-8648000102c1865d

Stanley, R., Al-Ansi, H., Weber, L.J., Snow, J., 2014. Spatial modeling of Jurassic Arab formation hierarchical carbonate depositional environment tracts as a guide to reservoir connectivity anisotropies: An example from the Dukhan Field, State of Qatar, in: Society of Petroleum Engineers - International Petroleum Technology Conference 2014, IPTC 2014: Unlocking Energy Through Innovation, Technology and Capability. pp. 1–15.

Steineke, M., Koch, T., 1935. Geological reconnaissance of the coastal plain of Hasa Province, northeastern Saudi Arabia. Dhahran.

Verwer, K., Oscar, M.T., Kenter, J.A.M., Della Porta, G., 2009. Evolution of a high-relief

 doi:10.20944/preprints202009.0366.v1

carbonate platform slope using 3D digital outcrop models: Lower jurassic djebel bou dahar, high atlas, Morocco. J. Sediment. Res. 79, 416–439. https://doi.org/10.2110/jsr.2009.045

Weijermars, R., 1999. Surface geology, lithostratigraphy and Tertiary growth of the Dammam Dome, Saudi Arabia: A new field guide. GeoArabia 4, 199–226.

Zhang, P., Pickup, G., Christie, M., 2008. A new practical method for upscaling in highly heterogeneous reservoir models. SPE J. 13, 68–76. https://doi.org/10.2118/103760-PA